Università
degli Studi di
Messina

**DEPARTMENT OF ENGINEERING**

PhD COURSE IN ENGINEERING AND CHEMISTRY OF
MATERIALS AND CONSTRUCTIONS - XXXVII CYCLE

---

# Novel CFD-Based Methods for the Characterization of Ventilated Planing Hulls and Analysis of Air Layer Distribution

***(SSD IIND-03/B)***

Candidate:

**Massimiliano Chillemi**

Supervisor:
**Prof. Filippo Cucinotta (SSD IIND-03/B)**

Co-Supervisor**:**
**Prof. Sebastian Brusca (SSD IIND-06/B)**

---

**A. Y. 2023/2024**

# Summary

# Abstract

Planing hulls are widely used in high-speed marine vessels due to their ability to reduce hydrodynamic resistance by lifting the hull partially out of the water at high speeds. This phenomenon minimizes the wetted surface area, allowing for greater speeds and fuel efficiency. A key technique employed to further reduce drag is the use of air cavity lubrication, where air is introduced beneath the hull to create a cushion between the hull surface and the water. This air cushion decreases friction, enhancing overall performance and lowering energy consumption.

The aim of the thesis is to explore the field of Air Cavity Ships by providing new tools for the assessment of the air cushion and for understanding its distribution under the hull in various operating conditions, addressing also the scale influence.

Two different hull designs were analysed. The first hull (hull A) served to validate a computational fluid dynamics (CFD) model using experimental data, providing a basis for examining how the air distribution beneath the hull varies with changes in scale. Once the CFD model was validated, the study shifted to a second hull (hull B). Through these analyses, a novel method for visualizing the air distribution beneath the hull was developed, incorporating the local thickness of the air cushion. Two new parameters were introduced to characterize hull

ventilation more effectively: the Air Direction Ratio and the Spray Rails Airflow Fraction.

In the final phase of the study, a propeller was placed behind the hull to evaluate the impact of its presence on hull ventilation. This analysis led to the calculation of the wake volumetric fraction, further refining the understanding of the interaction between hull ventilation and propulsion.

# 1. Introduction

The principle of Archimedes states that an object will float if it displaces a volume of water equal to its mass. When the object moves forward, it must push aside the displaced water. The forces generated during this movement arise from both friction against the surface of the object and inertial forces due to acceleration around the shape of the object.

At the water surface, these inertial forces create a wave pattern that affects the inertial load on the object. As speed increases, the wave pattern lengthens, causing a positive pitch attitude. When the length of the waves generated at the bow becomes twice the length of the object, it reaches a maximum trim angle. Further acceleration, if the form of the object allows, results in a reduction of the trim angle to around 2–4 degrees. The kinetic force acting on the underside of the object develops a vertical component that increases until, at a certain speed and depending on the form of the object, the mass is almost entirely supported by the kinetically generated lift—this is known as planing.

There are two main challenges in achieving the necessary force to accelerate an object to planing speed. The first challenge is frictional drag, which increases proportionally with the square of the velocity. The second challenge is that a shape suited for planing at high speed, typically with a wide lower surface, is not optimal for minimizing inertial drag forces at lower speeds when the object operates in 'displacement' mode.

Small objects may have a high power relative to their size to enable planing, but this approach is not economically viable for larger objects. Reaching a speed at the higher end of the displacement regime, where kinetic lift forces start to become significant, is challenging, especially when considering practical forms designed to carry dense bulk materials.

The two speed regimes cater to different market needs. Slower vessels encompass a wide range of types beyond just bulk carriers. Vessels that could benefit the most from reducing hull resistance are those for which fuel consumption represents a massive portion of operating costs. This includes tankers and bulk carriers at low speeds, as well as ferries and cruise ships within the high-speed range of displacement vessels. Reducing drag presents a particular challenge for vessels with relatively fine forms, as they have limited flat bottom area compared to their immersed surface area.

In the quest for greater efficiency and sustainability in maritime operations, the naval sector is increasingly focusing on resistance reduction strategies to enhance vessel performance and reduce environmental impact. The resistance to forward motion of a ship is fundamentally determined by three components: frictional drag, wave drag, and viscous drag. Notably, frictional drag, occurring due to viscous interactions between a ship's hull and the water, is a significant component, especially in contexts where wetted surfaces are extensive, such as in surface ships. Frictional drag contributes to 60%–70% of the total drag on cargo ships and roughly 80% on tankers.

In the context of reducing movement resistance in vessels, Computational Fluid Dynamics (CFD) provides a crucial tool for detailed analysis and optimization, especially within the realm of air lubrication techniques. CFD enables the simulation of complex interactions between water and naval structures, thereby facilitating the development of innovative solutions that enhance operational efficiency and meet sustainability challenges in the maritime sector. CFD is used to model the flow behaviour around the hull and within air cavities, assessing the effectiveness of different configurations in reducing resistance. Through CFD simulations, it is possible to predict how microbubbles, air films, or air cavities affect pressure distribution and velocity profiles along the hull, thus optimizing the design to maximize drag reduction. These simulations are crucial for understanding the delicate balance between the amount of air injected, the placement of injections, and the overall impact on the hydrodynamic resistance of the ship.

In this work, a literature review was conducted on the state of the art regarding air-assisted drag reduction technologies in Chapter 2, with two sections respectively dedicated to experimental studies and numerical studies. Then, in Chapter 3, the two studied hulls were introduced along with the parameters defined in the thesis and the setup of the CFD model. The results were collected and explained in Chapter 4. Chapter 5 addresses possible future developments and Chapter 6 presents the conclusions.

# 2. State of the art: air lubrication methods

Within the strategies for drag reduction, air lubrication techniques represent an important technological frontier. The classification of these techniques is divided into three principal categories. Microbubble Drag Reduction (MBDR) consists in bubbles (microbubbles) being injected into the boundary layer of water flowing along the hull, leading to a reduction in frictional drag by lowering the mean density and altering the velocity profile. Air Layer Drag Reduction (ALDR) employs a thin, continuous layer of air that is maintained between the hull and the water by injecting air along the hull surface. This layer creates a physical separation between the ship and the water, resulting in friction attenuation. Air Cavity Drag Reduction (ACDR), in contrast, establishes a stable air cavity or pocket is under the hull by pumping air into specially designed recesses. The air cavity replaces water contact over a portion of the hull, significantly reducing the wetted surface area and thus drag.

These techniques not only bring about improvements in terms of operational efficiency but also offer innovative responses to the pressing sustainability challenges in the maritime industry, reducing the fuel consumption of the vessels. It is essential to note that the transition from MBDR to ALDR mode and the subsequent implementation of ACDR are phenomena governed by the flow and pressure of air injected beneath the hull. The choice between these modes depends on the optimal balance between drag reduction efficacy and operational feasibility in relation to several types of ships and their specific operations.

The three mechanisms of air lubrication for drag reduction are depicted in Figure 1, showcasing MBDR (Figure 1a), ALDR (Figure 1b) and ACDR (Figure 1c).

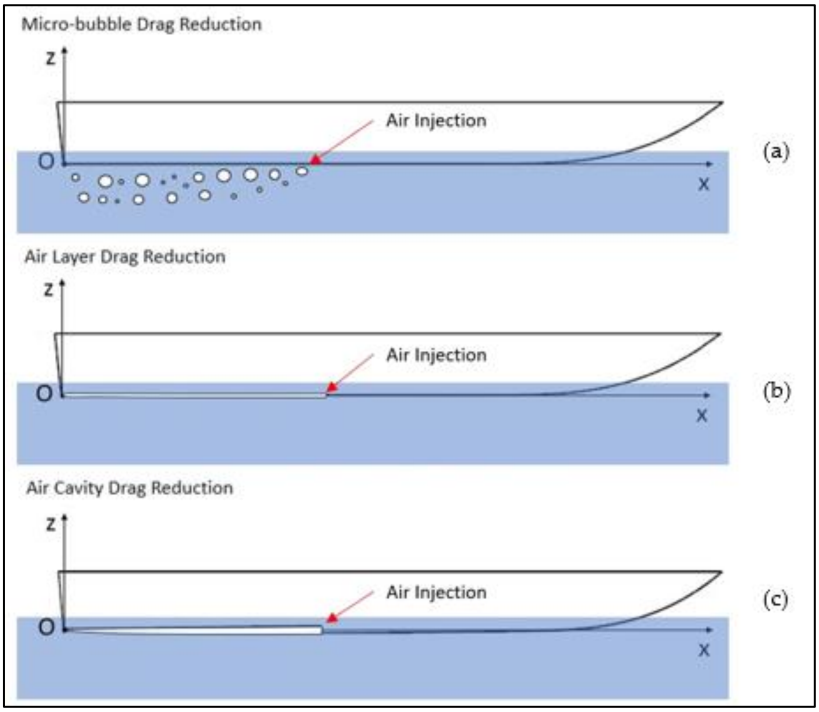

*Figure 1. Different techniques for reducing drag through air lubrication can be classified as follows: (a) the Microbubble Drag Reduction (MBDR) technique, (b) the Air Layer Drag Reduction (ALDR) technique, and (c) the Air Cavity Drag Reduction (ACDR) technique.*

The reported studies intend to deepen the understanding of air lubrication techniques, evaluating not just their efficiency in terms of drag reduction but also their overall impact on ship performance and the marine environment. In an era where sustainability has become a watchword for the industry, the potential of these technologies to contribute to a cleaner and greener future for the maritime sector is substantial.

Addressing the challenge of environmental sustainability is crucial across various design fields. The integration of air lubrication technologies should be considered within the broader context of ecological impact, energy consumption, and emissions reduction.

## 2.1 Experimental tests in literature

- *Micro-bubble drag reduction*

To investigate the reduction of friction in turbulent boundary layers of liquid flow due to the presence of bubbles, a series of experiments was conducted, starting with a study by Tsai et al. [1]. This research developed a model to predict the effectiveness of microbubble drag reduction techniques in a boundary layer on a flat plate. The experimental setup included a system for injecting microbubbles through porous materials and a resistance measuring system to assess the frictional drag on the flat plate, both with and without the presence of microbubbles. These experiments were performed in both a wind tunnel and a towing tank, with variations in flow velocity and air injection rates to evaluate the accuracy of the model's predictions. The findings of Tsai et al. indicated that the drag reduction effect predicted by the boundary layer mixture model is linked to the density ratio between the mixture and water, with an optimal air flow rate for each velocity tested in the towing tank.

Another study by Sanders et al. [2] examined the reduction of bubble friction in a turbulent boundary layer on a flat plate at high Reynolds numbers. Conducted at the US Navy's Large Cavitation Channel, this research used a 12.9-meter-long flat plate to create a turbulent boundary layer with a nearly zero pressure gradient. Air was injected at high volumetric rates through 40 µm sintered metal strips flush-mounted to the surface of the test model. Sanders et al. found that the surface shear stress measurements without air injection systematically underestimated frictional drag compared to expected values based on Schultz-Grunow friction line.

Elbing et al. [3] performed a series of experiments at the US Navy's William B. Morgan Large Cavitation Channel (LCC) to explore skin-friction drag reduction in a turbulent boundary layer (TBL) at high Reynolds numbers and large scales. These experiments involved injecting air through a line source into a TBL with a nearly zero pressure gradient, formed on a flat-plate test model that was either hydraulically smooth or fully rough. The study focused on two types of drag reduction phenomena: bubble drag reduction and air-layer drag reduction. Six drag balances were used to measure the longitudinal distribution of skin-friction drag reduction, with downstream-distance-based

Reynolds numbers reaching up to 220 million and test speeds of up to 20 m/s. Variables such as free-stream liquid velocity, gas injection rate, injection location, surface tension, and injector type were altered to assess their impacts.

Sayyaadi and Nematollahi [4] employed a different approach by using an experimental model to carry out controlled physical model experiments. At the Centre of Excellence in Hydrodynamics and Dynamics of Marine Vehicles at Sharif University of Technology, a series of experiments were conducted using a 70 cm long catamaran model made of plexiglass. The model was designed for air injection at three separate locations: the bow, midship, and stern areas. A crucial aspect of effectively utilizing the microbubble technique is accurately estimating the air injection rate. Although there is no direct conventional method to determine this rate, it can be inferred from indicators of boundary water flow. The experimental results showed that as speed increased, the peak drag reduction effect decreased, suggesting that the microbubble drag reduction technique is most effective for ships operating at lower speeds.

To enhance the effectiveness of frictional drag reduction using bubbles, Hyun Jin Park et al. [5] researched a novel method called Repetitive Bubble Injection (RBI), which differs from the traditional continuous bubble injection technique. RBI maintains drag reduction by generating swarms of bubbles, even with a low mean void fraction of injected bubbles in the turbulent boundary layer. The study involved detailed investigations of the enhanced drag reduction mechanism and the effectiveness of RBI by measuring the temporal variation of local wall shear stress, the velocity vector field of the liquid phase, and the gas-liquid interface in turbulent horizontal channel flows. The experimental setup included a transparent acrylic resin horizontal rectangular channel, using silicone oil as the working fluid. Two 4 MHz ultrasonic transducers were utilized to measure the internal flow structures, and the effectiveness of RBI was examined at Reynolds numbers exceeding 1200.

In another approach, Jacob et al. [6] investigated frictional drag reduction by introducing tiny amounts of microbubbles in a turbulent boundary layer over a flat plate. Their primary experiment, conducted in a 25-meter-long recirculating water channel, focused on understanding the reduction of viscous drag influenced by microbubbles. The microbubbles, with an average diameter similar to the local Kolmogorov length scale and a bulk void fraction of approximately 0.1%, were studied. The frictional drag on a 6-meter-long flat plate was measured, with microbubbles generated through electrolysis in a towing tank.

To assess the velocity components of the liquid phase, image-analysis techniques and a Feature Tracking (FT) algorithm were employed. The void fraction of the bubbles was estimated by calculating the projected bubble volumes within the measurement volume, and the distribution of bubbles in the near-wall region of the boundary layer was analysed [7].

Yanuar et al. [8] studied an alternative method for improving frictional drag reduction using bubbles in a high-speed vessel model, conducting experiments in a test basin with dimensions of 50 meters in length and 40 meters in width, with a constant water depth of 2 meters. These experiments involved a Froude number reaching up to 0.65. The central setup included a ship model attached to a load cell transducer above the baseline, allowing for unobstructed vertical movement. The total drag experienced by the model was recorded across different Froude numbers, and the ship model was towed using a wire rope to measure the longitudinal force exerted on the model at varying speeds, with freedom allowed for the model to pitch and heave.

Murai et al. [9] explored skin friction reduction using large air bubbles in turbulent flow within a horizontal channel. They found a negative correlation between local skin friction and local void fraction, with significant skin friction reduction observed at the rear of large individual bubbles. This study suggests that bubbles of a certain size can be more effective in reducing friction, offering new insights into the bubble-induced skin friction reduction process.

Kodama et al. [10] further investigated the effects of microbubbles on skin friction in ships using a water tunnel. They measured friction reduction and examined the relationship between local void fraction and friction reduction, also exploring the impact of ship size on the effectiveness of microbubbles, which could have implications for real-sized ships [11].

In pursuit of reducing hydrodynamic drag for ships at cruising speeds of 15-20 knots, Kumagai et al. [12] developed a novel energy-conserving apparatus. This device utilizes small bubbles generated by the Kelvin–Helmholtz instability phenomenon, injected via angled hydrofoils equipped with air introducers, strategically positioned beneath air release vents on the hull's surface. The apparatus aims to significantly reduce skin friction by injecting bubbles less than 0.5 mm in diameter into the turbulent boundary layer. Although the precise scientific mechanism behind this drag reduction is still being explored, empirical observations suggest that injecting bubbles into the turbulent domain attenuates Reynolds shear stress, with small bubbles naturally accumulating in the turbulent shear layer, thereby resisting turbulent diffusion and remaining effective in reducing drag.

A distinctive aspect of the system, referred to as the Winged Air Sensor Tube (WAIP) (Figure 2), is the incorporation of the aerofoil section NACA 653-618, which is positioned below the surface level and set at an angle of attack of 12 degrees. During the ship's forward motion, the hydrofoil redirects the water flow, generating a low-pressure area above the foil, which in turn draws atmospheric air into the water.

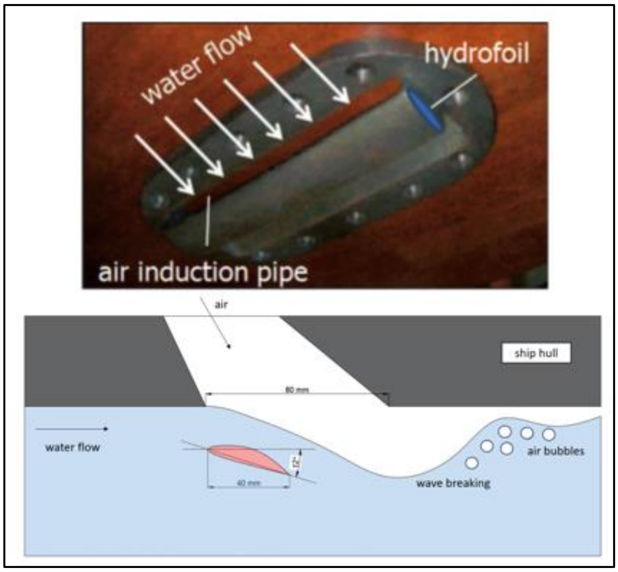

*Figure 2. Dimension and Kelvin-Helmholtz action of the WAIP system (a) and schematic illustration of the WAIP cross-section (b) (reproduced under a CC BY-NC-ND 3.0 DEED license).*

This setup not only reduces the pressure above the hydrofoil but also accelerates the water flow above it while slowing it down beneath, thereby creating vortices downstream of the foil and assisting bubble formation both at the interface between gas and water, and behind the trailing edge.

The test model ship, developed specifically for evaluating the WAIP system, comprises four sections, identified as A, B, C, and D in the Figure 3.

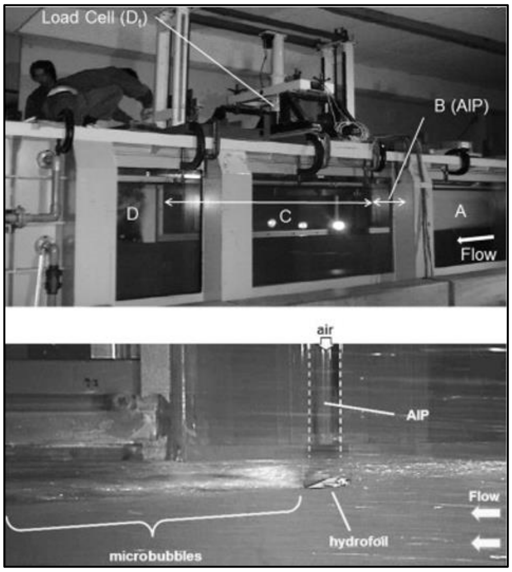

*Figure 3. Recirculating water flow (shown in a) (West Japan Fluid Dynamics Engineering Laboratory Co. Ltd.); microscopic bubbles produced by the hydrofoil system (shown in b) (reproduced under a CC BY-NC-ND 3.0 DEED license).*

The combined drag force experienced by sections B and C (notated as $D_t$) was assessed using a singular load cell. Concurrently, the drag impact on section B alone was independently gauged by a different load cell (marked as $D_o$). Thus, the drag exerted on the 2.6 m long acrylic flat panel (referred to as $D_b$) was calculated using equation (Eq. 1) from these data point.

The process of bubble generation and its contribution to decreasing the frictional drag on the downstream horizontal flat wall were meticulously investigated through experiments in a circulating water channel, where the flow velocity was established at 5.6 m/s to replicate the typical cruising speed of ships. Here, $B_h$ represents the horizontal width of the bubble-mixed layer, and $V$ denotes the flow velocity of the circulating water, with the water density indicated by $\rho$. For practical application to full-size ships, the total drag force $F_{total}$ (Eq. 2) that is acting on a flat plate with length $L$ by use of local friction factors with and without the air bubbles, represented by $C_f$ and $C_{f0}$, respectively.

$$D_b = D_t - D_0 \tag{1}$$

$$F_{Total} = D_t - \int_0^L \frac{1}{2} \rho V^2 C_{f_0} \left(1 - \frac{C_f}{C_{f_0}}\right) B_h dx \tag{2}$$

Tanaka et al. [13] investigated the effectiveness of Repetitive Bubble Injection (RBI) in reducing frictional drag within the turbulent boundary layers under a model ship, comparing it to Continuous Bubble Injection (CBI). This study aimed to understand how periodic fluctuations in bubble injection can lead to more efficient drag reduction than traditional continuous methods. The experiments were carried out using a 36-meter long flat-bottom model ship, towed at a speed of 8.0 m/s, where the RBI technique achieved a drag reduction ratio of up to 24%, marking a 5% improvement over CBI.

The researchers used high-frequency cameras to closely monitor the flow and distribution of bubbles beneath the ship, alongside direct measurements of local wall shear stress to assess the performance of the drag reduction methods. The study's analysis revealed that the downstream persistence of drag reduction was significantly enhanced by RBI. The effects of drag reduction could be observed up to 15 times farther downstream when compared to CBI, indicating a considerable extension of the effective drag reduction zone along the ship hull.

These findings suggest that the repetitive injection strategy alters bubble dispersion in a manner that prolongs the drag reduction effect along the hull, making it a potentially more efficient approach to reducing hydrodynamic resistance in marine vessels. The technique for generating and injecting the air cushion beneath the base of the passenger vessel hull is depicted in Figure 4. This method could represent a significant advancement in drag reduction technology, offering practical applications for improving the energy efficiency of ships.

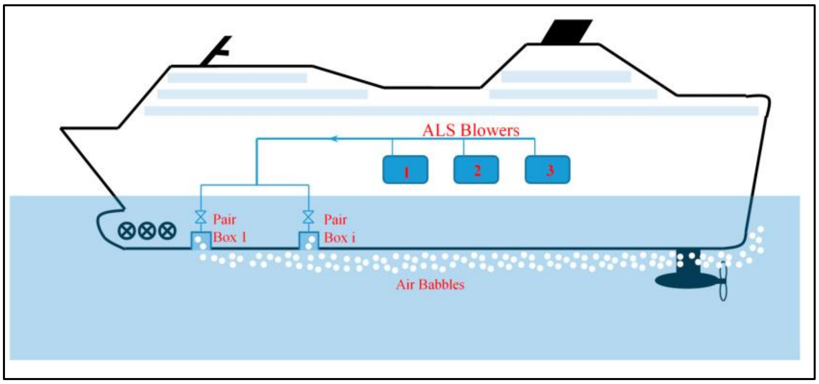

*Figure 4. Diagram of the system of introducing the air layer under the hull bottom of the passenger vessel-Air Lubrication System (ALS) (reproduced under a CC BY 4.0 DEED license).*

- *Air layer drag reduction*

The experimental method of air layering was investigated by Jang et al. [14]. The experiments were carried out using a flat plate measuring 7.5 m x 1.0 m x 8 cm, which was mounted horizontally in the test section of a water tunnel (Figure 5). Air was injected through a flush slit located near the front end of the plate, and changes in local frictional drag caused by the air layers were measured using two floating-plate-type friction sensors. Additionally, six independent air injection units were installed on the ship model, flush with the hull's bottom surface, to prevent any unwanted increase in drag. Compressed air was stored in receivers placed on the ship model deck, and the airflow to the injection units was controlled by regulated mass flow meters.

*Figure 5.* Flat plate in the water tunnel for generation of air layer (reproduced under a CC BY-NC-ND 4.0 DEED license).

The experiments demonstrated that a transitional air layer generated by air injection on the bottom of the hull can effectively reduce the frictional drag of ships. For a 66,000 DWT Supramax wide-beam bulk carrier, net power savings were estimated to be between 5% and 6%. This energy saving translates to an 8-10% reduction in effective power and a 7-9.5% reduction in delivered power due to less than a 1% loss in quasi-propulsive efficiency. The results suggest that air lubrication has significant potential for energy savings, provided there is no substantial performance deterioration in real sea conditions.

In another study conducted by Hao et al. [15], experiments were performed to investigate friction reduction using an air layer beneath a flat plate in a towing tank. The researchers observed the formation of the air layer and measured changes in drag. Drag and self-propulsion tests were also conducted on a ship model based on a 95,000 DWT container ship, utilizing the method of friction reduction through a lower cavity air layer. The formation of air layers was observed, and the estimated energy savings were calculated. The results indicated that the required power could be reduced by up to 15% in a full-scale ship, not accounting for the energy consumed during air injection.

In the study conducted by Wu et al. [16], the application of an air cavity on the bottom of a ship model for friction reduction was explored. The model featured a flat-bottom structure ideal for the implementation of air lubrication drag reduction (ALDR) technology. Two air injection devices were used to form an air layer within the cavity, and the depth of the cavity was varied to study its effects on the ship's drag and propulsion. Air was injected through holes in the base plate of each device, and the cavity depth was adjusted to examine its impact on the ship's drag.

To further understand the impact of air flow rate and inflow velocity on air layer formation, the non-dimensional air flow rate coefficient (Eq. 3), $C_q$, is defined using the air flow rate ($Q$), inflow velocity ($V$), transverse width of the air injection entrance ($B$), and the thickness of the boundary layer at the air injection entrance without air injection ($\delta$).

$$C_q = \frac{Q}{VB\delta} \tag{3}$$

The proposed coefficient helps relate the air injection flow rate to the ship velocity, which is crucial for accounting for how different speeds affect drag reduction. In the study, the ship model's relative drag reduction rate was observed in relation to wavelength, considering different cavity depths and air flow coefficients ($Cq$ values of 0.112, 0.168, and 0.224) at a Froude number of 0.155. It was noted that the change in drag reduction rate with wavelength followed the same trend across different $Cq$ values. Generally, the relative drag reduction rate was higher in the 25 mm cavity and in long waves, reaching over 30% in long waves at a *Cq* of 0.224, which was higher than in calm water.

The study also found that the presence of the cavity increased drag, with a 13.9% increase at a cavity depth of 25 mm at the design speed. The investigation highlighted that ALDR technology effectiveness can vary with the mode of air injection, showing no direct correlation between friction reduction and the mode of injection in this experiment. When a 25 mm cavity was continuously supplied with air at an airflow coefficient *Cq* of 0.224 in calm water, there was approximately a 20% reduction in absolute drag at the ship's design speed, with the drag reduction effect persisting even in long waves.

In a different study, Elbing et al. [3] explored air drag reduction using a 12.9 m long flat-plate model with a 13 mm protrusion at the air injection site. They tested the effect of vortex generators on the boundary layer, both with and without vortex generators. A novel scaling for critical air flux was proposed, based on single bubble analysis in shear flow. This scaling, which considers the ratio of buoyancy to turbulent shear forces, unified data across different surface conditions and air injection methods.

Yanuar et al. [17] studied the use of porous media for injecting microbubbles and air layers to reduce drag on a self-propelled barge model. They used a 30 cm wide porous medium with an average hole diameter of 100 µm to generate bubbles and layers beneath the hull. The study found that these microbubbles and air layers significantly reduced water resistance, demonstrating potential efficiency improvements for maritime transport.

Aljallis. et al. [18] investigated the reduction of skin friction drag using superhydrophobic-coated flat plates in high Reynolds number boundary layer flows. They coated aluminium flat plates with hydrophobic nanoparticles to create surfaces with varying contact angles and hysteresis. Testing in a high-speed towing tank revealed significant drag reduction in certain conditions, attributed to the shear-reducing effects of the air layer on the superhydrophobic surface.

Additionally, the study explored basic drag reduction by using a traversing probe system to assess void fraction and gas-phase velocity profiles. Despite variations in vortex generator configurations, the measurements showed a consistent interfacial velocity profile, like single-phase flows. Discrepancies in void fraction profiles were observed, likely due to measurement uncertainties near the wall.

- *Air cavity drag reduction*

In the study by Slyozkin et al. [19] a simplified flat plate model was used to explore the impact of air cavities on hydrodynamic drag reduction. The experiments were conducted in the Emerson Cavitation Tunnel at Newcastle University, with the main goal of understanding how the length and volume of air cavities influence drag reduction. The results indicated that air cavities could significantly reduce hydrodynamic drag, providing valuable insights into the relationship between cavity dimensions and drag reduction. This research enhances the understanding of air cavities and their practical applications in marine transport.

Another study by Butterworth et al. [20] assessed the effect of air cavities on reducing hydrodynamic resistance for a ship's hull. They used a 2.2-meter container ship model, modified to include an air cavity, and conducted tests in a towing tank. The experiments aimed to evaluate the performance of the air cavity system in reducing drag and its effectiveness in real-world conditions.

The study found that the introduction of an air cavity into the ship hull led to a variable reduction in resistance, which was influenced by both the air flow rate and the ship velocity. The research included tests on static stability, resistance, and motion response to assess the impact of the air cavity on the ship performance. The results indicated a minor effect on static stability but an increase in hull drag by 10% compared to the standard model. Despite this, drag reduction was achieved, with a 4% saving noted even with only a 5% reduction in the wetted surface area. Limited motion response tests suggested that the air cavity might induce nonlinear vertical motion behaviours, potentially affecting drag under specific wave conditions.

In the research conducted by Agostino De Marco et al. [21], both experimental tests and numerical simulations were used to study a stepped hull model's hydrodynamics. The tests were carried out in a towing tank and focused on drag, dynamic sinking, and trim angle of the model. Numerical simulations applied various mesh techniques to model hull motion and water flow. The experiments revealed complex vortical flow phenomena in the unwetted area behind the step of the hull, especially at speeds above 2.36 m/s. These vortices, originating from air spillage at the sides of the step, displayed intricate three-dimensional behaviour. The "down-thrust" method used in the tests provided precise data on drag, dynamic sinking, trim, and the dynamic wetted surface of the hull, offering significant insights into the hydrodynamic behaviour of stepped hulls.

A notable contribution to the study of Air-Cavity Ship (ACS) systems is presented in the work by Cucinotta et al. [22]. This research focused on evaluating different air cavity configurations in a planing hull through towing tank tests (Figure 6). Four hull models (Models A, B, C, and D) were meticulously designed and tested at varying speeds and air flow rates, using the Froude method for evaluation. The results from these tests contributed valuable insights into the effectiveness of different air cavity configurations in reducing hydrodynamic drag and improving the efficiency of planing hulls.

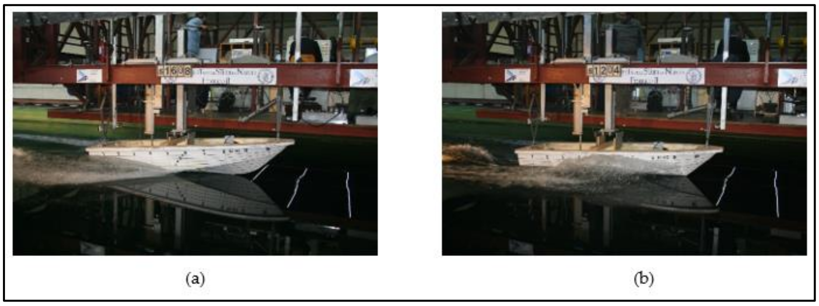
(a)
(b)

*Figure 6.* (a) towing tank test with air injection, (b) test without air injection.

From the analysis, it is evident that air cavities in planing hulls significantly reduce drag compared to tests without air. The energy savings become more pronounced at speeds exceeding 5.04 m/s, with Model B being the most efficient across all tested conditions of speed and air flow. For Model C, a minimum air flow rate of 7500 liters per minute is required at 5.04 m/s to observe a meaningful impact of air injection. The air entrainment coefficient (CQ), with a value around 1, indicates a stationary air cavity. The study also found that more complex hull geometries do not necessarily improve performance, as planing hulls naturally create low pressure at the bottom, which helps maintain the air layer. Overall, the study offers a comprehensive analysis of how different air cavity configurations affect drag and hydrodynamic behaviour in planing hulls.

In another study by Song et al. [23], conducted in a towing tank measuring 135 meters long, 7 meters wide, and 3.6 meters deep, a model made from wood-plastic panels and equipped with a transparent plexiglass window was tested. The study explored various speeds and initial stern inclination angles with an air cavity pressure of 50 kPa to evaluate its impact on drag. The model underwent drag tests under different air cavity pressures and inclination angles. Data on drag, pitch, and inclination angles were collected in real-time using a dynamometer and sensors.

The findings indicate that the initial stern inclination angle plays a crucial role in reducing drag effectively, with this angle needing to be adjusted based on speed. Drag decreases with increasing air pressure, stabilizing once optimal pressure is reached. At 50 kPa and a displacement of 125 tons, the minimum drag, showing an 18.3% reduction, occurs at a 2.5 degrees angle. These preliminary tests are vital for validating the feasibility of the air cavity concept and for minimizing costs and time.

## 2.2 Numerical simulations in literature

- *Micro-bubble drag reduction*

Numerical simulations of drag reduction using microbubbles often employ various turbulence models, including Reynolds-

Averaged Navier-Stokes (RANS), Large Eddy Simulations (LES), and Direct Numerical Simulations (DNS).

In Zhao et al.[24], an Eulerian-Eulerian two-fluid model is used in OpenFOAM to simulate both the liquid and bubble phases. The standard k-ε turbulence model applies to the liquid phase, while a separate model handles the gas phase. The study employs the Interfacial Area Transport Equation to calculate bubble sizes, incorporating bubble coalescence and breakup dynamics.

Mohanarangam et al. [25] use a similar Eulerian-Eulerian framework with the Multiple-Size Group (MUSIG) approach, which resolves various bubble sizes and considers bubble coalescence and breakup. This study uses standard k-ε and Shear Stress Transport (SST) models for turbulence in the liquid phase, and a zero-equation turbulence model for microbubbles. Validation against experimental data highlights the MUSIG model's accuracy in representing bubble dynamics in drag reduction scenarios.

Gamal et al. [26] evaluate microbubble drag reduction effects on container ships using the realizable k-ε model within the RANS framework. The study assesses varying Froude numbers and air flow rates to gauge drag reduction.

Xia et al. [27] explore microbubble drag reduction for underwater vehicles during pitching movements, utilizing a

Population Balance Model (PBM) to simulate bubble aggregation and breakup. The Shear Stress Transport (SST) k-ω model addresses turbulence, and experimental validation confirms the numerical model's accuracy in predicting drag and lift coefficients under different conditions. An et al. [28] conduct a comprehensive numerical investigation of microbubble drag reduction on an axisymmetric submerged body using the Eulerian multiphase model. The study, employing the k-ω turbulence model, examines how microbubble distribution affects drag. It finds that smaller bubbles, while enhancing frictional drag reduction, can increase pressure drag due to flow separation. Xiaosong et al. [29] use LES within the Euler framework to simulate the liquid phase, tracking bubbles using kinematic equations. The study features a two-way coupled algorithm to handle interactions between the liquid and bubble phases. A Gaussian bubble volume distribution scheme enhances accuracy by averaging bubble volumes into the grid. This approach is validated against experimental data and other simulations, demonstrating improved accuracy in tracking bubble behaviour. Xu et al. [30] and Pang et al. [31] use DNS to resolve turbulence. Xu et al. investigate the impact of microbubbles on turbulent drag in channel flow, employing DNS to simulate turbulent flows seeded with rigid spherical bubbles. The study, using the Force-Coupling Method (FCM), examines different bubble sizes and void fractions, focusing on drag force and mean pressure gradient changes. Pang et al. also use DNS to explore microbubble effects in a horizontal channel, tracking bubble trajectories with Newtonian motion equations. The study investigates low drag-reduction conditions, considering factors such as liquid-phase velocity changes and turbulence intensity, with typical velocity vectors illustrating suppressed liquid phase motions compared to pure liquid. Figure *7* shows the typical instantaneous velocity vectors at a cross section in the y–z plane of the channel. It clearly illustrates that, throughout the channel, the ejection and sweep motions of the liquid phase are suppressed compared to those of the pure liquid.

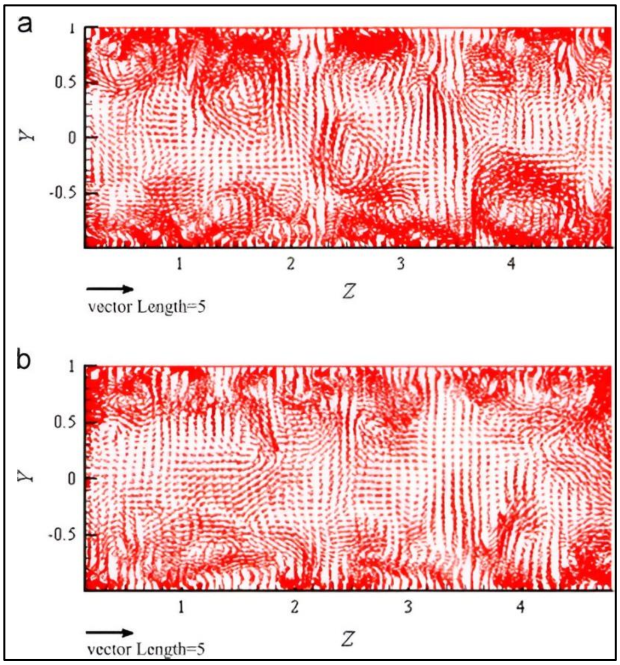

Figure 7. Instantaneous velocity profile at a y–z plane. (a) Pure liquid and (b) liquid phase ([31] reproduced under a CC BY license).

- *Air layer drag reduction*

Montazeri and Alishahi [32] introduced a novel approach that integrates linear stability analysis with Unsteady Reynolds-Averaged Navier-Stokes (URANS) modelling. This method aims to enhance CFD accuracy for turbulent flows involving air layers and predicts flow instabilities more effectively. The study is validated against experimental data and demonstrates improved modelling of two-phase flows and accurate instability predictions.

Zhang et al. [33] investigated the drag reduction potential of a Winged Air Induction Pipe (WAIP) for ship hulls using OpenFOAM.

Their study focuses on various parameters such as the hydrofoil's submergence depth, angle of attack, and air inlet pressure. The numerical results for drag reduction are compared with experimental data to validate the effectiveness of the WAIP device.

Hao and Yongpeng [34] combined the RANS model with the Volume of Fluid (VOF) method to explore the dynamics of air layers within air cavities. Their study examines how different cavity parameters influence the morphology of air layers, providing insights into how these factors affect drag reduction (Figure 8).

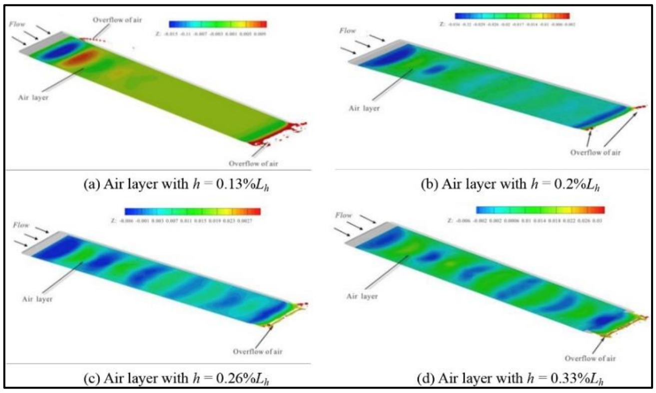

(a) Air layer with $h = 0.13\%L_h$ (b) Air layer with $h = 0.2\%L_h$

(c) Air layer with $h = 0.26\%L_h$ (d) Air layer with $h = 0.33\%L_h$

Figure 8. Influence of air cavity depth on the air layer distribution (reproduced under a CC BY license).

Ye et al. [35] also utilized the RANS model to analyse air layer effects on drag reduction, focusing on the interaction between the air and fluid phases. Their CFD simulations aim to refine the understanding of how air layers influence drag and improve the accuracy of predictions in various operational conditions.

The analysis relies on Reynolds-Averaged Navier-Stokes (RANS) equations to model the flow around ships, with turbulence captured using the RNG k-ε model. This refined version of the standard k-ε model provides improved accuracy in handling strain rates and gradient flows typical of turbulent boundary layers and separated flows.

The simulations reveal that the air layer effectiveness in reducing drag depends significantly on water depth. In deeper water, the air layer remains stable and continuous beneath the ship, leading to substantial frictional drag reduction. However, in shallow and ultra-shallow waters, the air layer becomes fragmented and disturbed, reducing its drag-reducing efficacy. The results indicate that in deeper water, drag reduction can reach up to 30% under optimal conditions, whereas in shallow waters, the effectiveness diminishes considerably due to increased disturbance near the ship's hull. X. Zhang [36] examines the efficiency of various cavity designs for drag reduction on a flat plate using Large Eddy Simulation (LES) and the Volume of Fluid (VOF) method. The study focuses on the air-water interface and evaluates how factors such as injector direction and front wedge height influence air layer formation and drag reduction. Findings indicate that reducing the wedge height significantly improves the stability and uniformity of the air layer, thereby enhancing drag reduction.

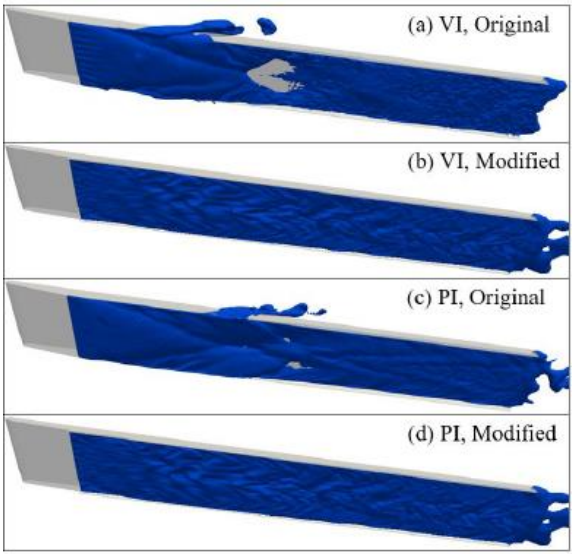

Figure 9. The effect of modified wedge block height on the air layer shape ([36] reproduced under a CC BY license).

Xu et al. [37] conducted a study on utilizing the steady Coanda effect to control ship airflow, aiming to reduce drag and manipulate the air wake around the vessel. The research employed Large Eddy Simulation (LES) with the Wall-Adapting Local Eddy (WALE) viscosity model to enhance the flow control of a baseline Chalmers ship model (CSM). The model was modified by adding Coanda surfaces and jet slots at specific locations on the ship to improve airflow manipulation.

The LES approach, combined with the WALE model, was chosen for its capability to handle large-scale turbulence and instabilities, which are crucial for accurate simulations of airflow control. The numerical model's effectiveness was validated using experimental data from tests on the unmodified baseline ship model.

The study tested four configurations: one without jets and three with different jet activation positions (roof, sides, and a combination). Results showed that the roof jet configuration notably improved the Coanda effect, directing airflow more efficiently towards low-speed areas on the deck. This configuration resulted in reduced drag and altered air wake characteristics, which are crucial for applications like helicopter landings on ship decks. The study concluded that manipulating airflows with Coanda surfaces and jets can significantly enhance ship aerodynamics by reducing drag and stabilizing the air wake, with the roof jet providing the most substantial benefits.

Kim et al. [38] explored the drag reduction mechanism of air layers (ALDR) through direct numerical simulations (DNS). The study examined various air injection rates and their effects on the stability and efficiency of ALDR. By comparing high and low air injection rates, the research investigated how these rates influence the stability of the air layer and its impact on drag reduction. Additionally, the theoretical analysis of air layer stability using the Orr-Sommerfeld equations was included. The findings indicated that the presence of the air layer affects the mean reattachment length of the flow, highlighting how air injection alters flow characteristics and contributes to drag reduction.

- *Air cavity drag reduction*

Lotfi et al. [39] conducted simulations of a ship's free heave and pitch movements, focusing on key parameters such as drag, lift, running draft, dynamic trim angle, and wetted area. They compared these parameters with experimental data and semi-empirical methods. The computational fluid dynamics (CFD) simulations utilized the $k-\varepsilon$ turbulence model to account for turbulent flow effects. The study also explored the wake profile and reattachment locations in relation to the stepped hull design.

Cucinotta et al. [40] evaluated the effectiveness of the RANS CFD approach in studying ship performance with and without air injection. The research was divided into two phases: the first phase focused on drag curves without air injection, while the second phase examined air distribution under the hull with air injection. The Shear Stress Transport (SST) k-ω turbulence model was employed to simulate air-water interactions and assess the impact of air injection on drag and air distribution. Results were compared with experimental data to validate the CFD approach.

In another study, Cucinotta et al. [41] used the k-ε turbulence model to simulate the effects of varying air bubble diameters on frictional drag and hydrodynamic efficiency in flat plates, a crucial component in Air-Cavity Ship (ACS) design. The research aimed to optimize the air cavity system for improved ship performance.

Cucinotta et al. [42] investigated the shape of the bottom of a multi-stepped air cavity planing hull through both experimental and numerical methods. They varied velocity and airflow rates to analyse how the Froude number affects the air cushion shape. The study looked at frictional drag and airflow path lines, which are challenging to assess with traditional experimental methods. The SST k-ω turbulence model was used in their CFD simulations.

Cucinotta et al. [43] examined the impact of longitudinal rails on a single-stepped planing hull with forced air ventilation. The study compared towing tank tests with CFD analyses to evaluate how these rails affect drag and wetted surface. The simulations employed the SST k-ω model with multiphase models for high-resolution capture of air-water interfaces. The analysis aimed to understand the influence of longitudinal rails on hull performance, particularly in terms of drag reduction and air-water interaction (Figure 10).

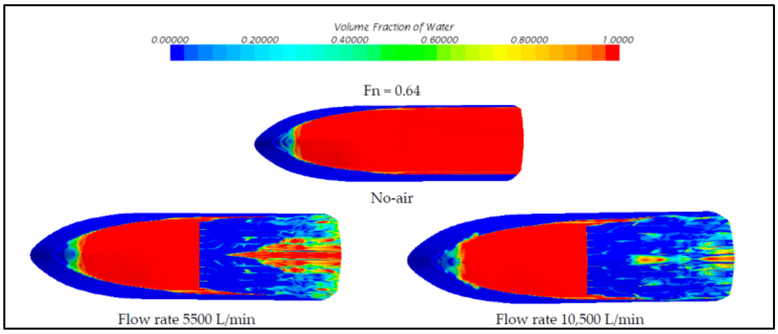

*Figure 10***.** Wetted surface in three different conditions: no-air and injection of the air to the minimum tested flow rate ([43] reproduced under a CC BY license).

Fang et al. [44] investigated the effectiveness of air cavity technology in reducing drag and its impact on the heeling stability of planing hulls. The study utilized three-dimensional Reynolds-Averaged Navier-Stokes equations combined with the Volume of Fluid method (RANS-VOF) and applied the SST k-ω turbulence model to analyse fluid dynamics around the air cavities under the hull. The research assessed how various forms of air cavities, such as meniscus growth cavities (MGC) and bottleneck stable cavities (BNSC). affect drag reduction and stability. Key findings include the identification of critical ventilation rates for optimal drag reduction and the negative impact of excessive ventilation, which can destabilize the air cavity by enlarging the tail air leakage opening. At a heel angle of around 2 degrees, the air cavity's shape deteriorates, diminishing drag reduction benefits. The study highlighted that while air cavities effectively reduce drag, they also affect heeling stability, necessitating careful management of ventilation rates and heel angles to ensure operational safety.

Mukha et al. [45] evaluated a planing yacht’s performance with air cavity technology using the Large Eddy Simulation (LES) model. The study was divided into two parts: the first assessed drag curves without air injection, and the second explored the effects of air injection under the hull. The research compared CFD results with experimental data to analyse streamlines, air distribution, and the wetted and ventilated areas of the hull. This comparison helped understand the relationship between flow rate, hull velocity, and air distribution, providing insights into hull geometry adjustments for better air layer accommodation.

Matveev et al. [46] explored artificial cavitation by introducing air under a vessel to reduce drag. The study examined the interplay between cavitation and ship propulsion, presenting a comprehensive model and parametric analysis to maximize efficiency. It concluded that while artificial cavitation can significantly reduce drag, the actual benefits depend on the complex interactions between cavitation and the propulsion system, underscoring the need for a detailed understanding of these interactions to fully utilize cavitation for drag reduction.

Yang et al. [47] found that the air cavity formed under a stepped planing hull significantly reduced the hull’s wetted area, decreasing resistance and improving performance. Their CFD simulations provided insights into how air cavities influence hydrodynamics, suggesting potential directions for optimizing hull design.

Amromin [48] highlighted that the interaction between ship bottom air cavities and boundary layers could lead to optimized drag reduction if managed properly. The study emphasized the importance of understanding these interactions to accurately predict and control air demand for ventilated cavities, which is essential for achieving effective resistance reduction and enhancing overall ship efficiency.

# 3. Materials and methods

## 3.1 Novelties overview

In this thesis, two different hulls were studied. The first hull was used to validate the model with experimental data, enabling the analysis of how the air distribution beneath the hull varies with changes in hull scale. Once the CFD model was validated, a second hull was analysed. From these investigations, a novel method for visualizing the air beneath the hull was developed, which accounts for the local thickness of the air cushion. Additionally, two parameters were defined to better characterize the hull's ventilation: the Air Direction Ratio and the Spray Rails Airflow Fraction. Finally, an additional analysis was conducted by introducing a propeller behind the hull and assessing its influence on the ventilation, leading to the definition of the thrust deduction factor and the wake volumetric fraction.

## 3.2 Studied hulls overview

The studied hulls are typical planing hulls. They are designed to lift and skim on top of the water at high speeds, rather than displacing water. The main characteristics of planing hulls are a flat or V-shaped bottom that allows them to rise and glide over the water surface. An important dimension for this kind of feature is the angle of deadrise. Another characteristic of these hulls is the hard chine, it is a sharp edge along the bottom sides of the hull. Usually, these types of hulls are resigned with an emphasis on reducing water resistance and maximizing lift.

### 3.2.1 Hull A overview

Figure 11 shows the geometry of hull A. This configuration has a cavity for air injection and the insertion of longitudinal rails. A great problem for the stability of the air-cavity is the escape of the air in transversal direction, due to the V-shape of the hull. The presence of longitudinal rails allows channelling the flow reducing the possibility to escape from transversal direction.

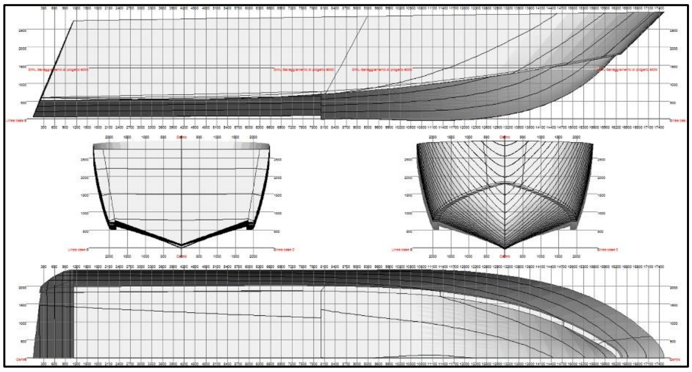

*Figure 11. Hull A geometry*

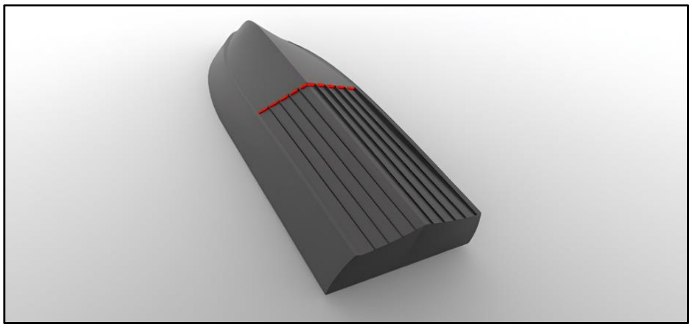

*Figure 12. Hull A geometry, spray rails*

The main dimensions of the hull are listed in Table 1.

*Table 1. Hull A dimensions*

| **Definition** | **Symbol** | **Value** | **Unit** |
|---|---|---|---|
| Overall Length | *LOA* | 16.20 | m |
| Waterline Length | *WTL* | 14.94 | m |
| Projected Beam Transom | *BPT* | 3.66 | m |
| Projected Maximum Beam | *BPX* | 3.72 | m |
| Deadrise Angle | $\beta$ | 20 | ° |
| Full Load Displacement | $\Delta$ | 36 | t |
| Longitudinal Centre of Gravity | *LCG* | 5.88 | m |
| Vertical Centre of Gravity | *VCG* | 1.56 | m |
| Number of Steps | $N_{ST}$ | 1 | – |
| Position of the step relative to the transom | $L_{ST}$ | 8 | m |
| Step Dimensions – Half Basis x Height | $B_{IN} \times H_{IN}$ | 1.6 × 0.09 | m × m |

### 3.2.2 Hull B overview

The fundamental geometric characteristics of the planing hull under investigation are reported in Table 2.

The original hull does not include a step that was added to be able to inject the air. All the main dimensions of the original hull have been kept the same. The hull has a constant deadrise angle equal to 20° along the vessel length.

*Table 2. Hull B dimensions*

| **Definition** | **Symbol** | **Value** | **Unit** |
|---|---|---|---|
| Overall Length | $LOA$ | 14.5 | m |
| Waterline Length | $LH$ | 13 | m |
| Projected Beam Transom | $BPT$ | 3.8 | m |
| Projected Maximum Beam | $BPX$ | 3.93 | m |
| Depth | $DPT$ | 2.23 | m |
| Draft | $DFT$ | 0.76 | m |
| Deadrise Angle | $\beta$ | 20 | ° |
| Full Load Displacement | $\Delta$ | 15 | t |
| Longitudinal Centre of Gravity | $LCG$ | 4.2 | m |
| Vertical Centre of Gravity | $VCG$ | 1 | m |
| Number of Steps | $N_{ST}$ | 1 | – |
| Position of the step relative to the transom | $L_{ST}$ | 4.4 | m |
| Step Dimensions – Half Basis x Height | $B_{IN} \times H_{IN}$ | 1.72 × 0.055 | m × m |

The value of the beam at the transom is 3.8 m and the beam change along the vessel reaching the maximum value of 3.93 m. The hull geometry is represented in Figure 13.

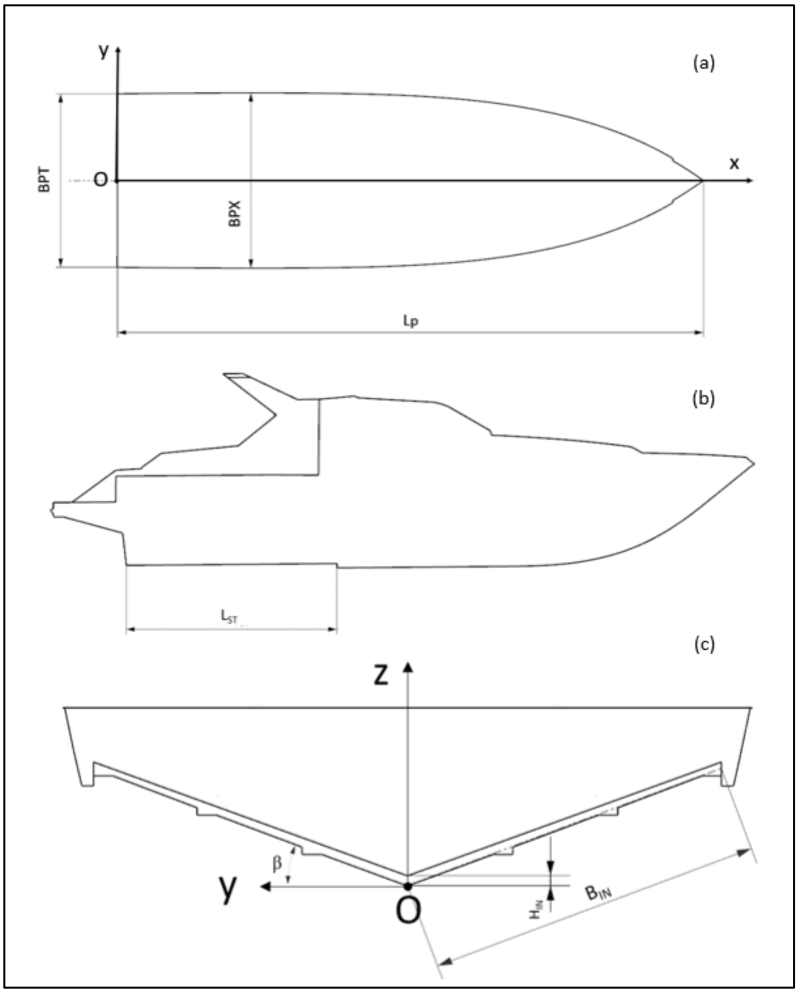

*Figure 13. From top to bottom: Top view of the hull (a), side view with the stepped hull (b), the rear view (c)*

## 3.3 Towing tank tests on scaled Hull A

A towing tank test is commonly employed to evaluate the hydrodynamic behaviour of marine vessels, such as ships, submarines, and offshore structures. This process involves testing scaled-down models in a controlled water environment. The towing tank itself is a long, water-filled basin equipped with precise measurement tools and a towing carriage that moves the model at set speeds.

The key objectives of these tests are to assess resistance, propulsion efficiency, seakeeping capabilities, and manoeuvrability. Resistance tests provide data on drag forces, offering insight into how the vessel will perform in varying water conditions. Propulsion tests evaluate the effectiveness of the propulsion system, while seakeeping tests focus on the vessel’s stability and performance in waves. Manoeuvrability tests examine how well the vessel can handle turns and directional changes. Due to the impracticality of testing full-scale vessels, scaled models, often in the range of 1:5 to 1:100, are used. These models are built with great accuracy to ensure they represent the vessel geometry and physical characteristics. Once test data is gathered, it must be extrapolated to predict the full-sized vessel performance using standardized ITTC ’57 scaling methods. The tests were conducted in the University of Naples towing tank, which has a total length of 137.2 m, a width of 9 m and a depth of 4.2 m. It is equipped with a towing carriage with a maximum forward speed of 10 m/s to perform model testing for power prediction, seakeeping, and unconventional hydrodynamics experiments. The dimensions of the towing tank and the maximum speed of the carriage allow for relatively large hull models and provide very good correlation between tank results and real sea conditions. The carriage is managed by eight asynchronous motors of 18 kW each delivered by independents inverter system. In the tests conducted for this study, a 1:6 scaled model of Hull A was examined at Froude numbers of 0.51, 0.77, 1.02, and 1.36, both with and without air injection at a fixed flow rate of 8500 l/min (Figure 14).

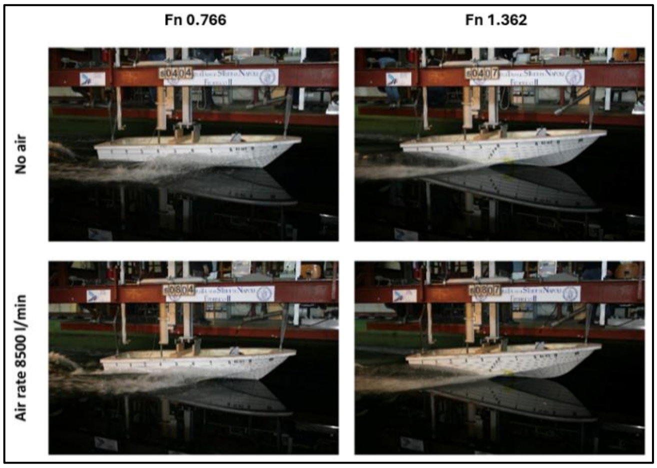

*Figure 14. Tests performed on scaled Hull A*

The data obtained from the towing tank test referred to the scaled model and the full scale performance prediction are listed from Table 3 to Table 6.

*Table 3. Towing tank results without air injection*

| **Fn** | **$V_M$ (m/s)** | **$RT_M$ (kN)** |
|---|---|---|
| 0.511 | 2.520 | 0.149 |
| 0.766 | 3.780 | 0.220 |
| 1.022 | 5.040 | 0.266 |
| 1.362 | 6.720 | 0.302 |

*Table 4. Towing tank results with an air injection of 8500 l/min*

| **Fn** | **$V_M$ (m/s)** | **$RT_M$ (kN)** |
|---|---|---|
| 0.511 | 2.520 | 0.150 |
| 0.766 | 3.780 | 0.211 |
| 1.022 | 5.040 | 0.250 |
| 1.362 | 6.720 | 0.247 |

*Table 5. Full scale ITTC prediction without air injection*

| **Fn** | **$V_S$ (m/s)** | **$V_S$ (kn)** | **$RT_S$ (kN)** |
|---|---|---|---|
| 0.511 | 6.172 | 12 | 31.721 |
| 0.766 | 9.259 | 18 | 45.923 |
| 1.022 | 12.345 | 24 | 54.354 |
| 1.362 | 16.461 | 32 | 59.567 |

*Table 6. Full scale ITTC prediction with an air injection of 8500 l/min*

| **Fn** | **Vs (m/s)** | **Vs (kn)** | **RTs (kN)** |
|---|---|---|---|
| 0.511 | 6.172 | **12** | **15.341** |
| 0.766 | 9.259 | **18** | **21.476** |
| 1.022 | 12.345 | **24** | **25.438** |
| 1.362 | 16.461 | **32** | **25.200** |

## 3.4 CFD Setup

The CFD model is useful for solving the field of velocity and pressure around the hull, the motion of the hull in terms of trim and sinkage. The fluid is considered viscous and incompressible, the interaction between the water and the air is considered thanks to a simulation multiphase. Simulations were conducted using Simcenter STAR-CCM+.

The CFD model, as previously mentioned, is shared between both hulls. It was validated, as demonstrated in Appendix A, through tests conducted on Hull A both on 1:6 scale and full scale and subsequently used to analyse Hull B. The dimensions in the model are consistently expressed relative to the fundamental parameters of the examined hull, and the boundary conditions are analogous for both cases. The images of the setup provided in the study specifically refer to Hull B.

The Unsteady Reynolds Averaged Navier Stokes (URANS) equations are solved using an implicit solver with an adaptive time step calculated to satisfy the condition of the Courant number being equal to or less than 1. To solve the pressure and velocity fields, a Segregated Flow approach is employed, with the momentum and continuity equations connected through a predictor-corrector method. For all simulations, the turbulence model employed is the Realizable k-ε Two-Layer model. The algebraic system of equations is solved using an Algebraic Multigrid method. The Hybrid method Gauss-Least Square (Gauss-LSQ) is utilized to solve gradients during the discretization process, combining aspects of the Gauss and Least Square methods. A time-marching approach is adopted for each simulation to capture unsteady phenomena, employing first-order temporal discretization. In addition to the Navier-Stokes equations, an additional transport equation is solved for the volume fraction of the two immiscible fluids. The Volume of Fluid method (VoF) is considered for this purpose. The High-Resolution Interface Capturing (HRIC) scheme is employed for convection in the VoF method, ensuring a sharp interface between the immiscible fluids. During the simulations, the planing hull is allowed to pitch and heave. To accurately capture the strong interaction between air and water, multiphase interaction is incorporated with a surface tension of 0.072 N/m imposed between the two fluids. An important concern in these studies is numerical ventilation. To recover and prevent ship hull ventilation, a User-Defined Slip Velocity approach was implemented within the VOF framework. Numerical ventilation, which refers to the undesirable mixing of phases, is a common issue in marine simulations. This Slip Velocity approach, integrated within the VOF framework, functions by algebraically computing distinct velocities for the two phases when they coexist, thereby enabling the separation of air from water and restoring the interface. A distinguishing feature of the VOF Slip Velocity model, which sets it apart from other techniques aimed at reducing numerical ventilation, is its physical basis. This aspect allows for its utilization in scenarios where the presence of air is expected in the solution, such as in stepped hulls. The method is presented in detail in [49].The Dynamic Fluid Body Interaction solver is activated, enabling the evaluation of hydrodynamic forces within each time step and solving the rigid body equations (Newton second law) to determine hull sinkage and trim. The mesh motion resulting from the hull movement is managed using the Overset technique, which is more advantageous for high-speed ships than the morphing methodology. This technique ensures minimal degradation of cell elements, particularly at high trim angles, while maintaining high accuracy near all boundaries. Table 7 provides a summary of the setup for the numerical simulation.

*Table 7. Physics models of the CFD simulation*

| **Physics model** | |
|---|---|
| **Discretization method** | Finite volume method |
| **Solver** | Implicit Unsteady |
| **Approach** | Segregated Flow |
| **Continuity and Momentum Equation coupling** | SIMPLE - Algorithm |
| **Convection Term** | $2^{nd}$ Order |
| **Turbulence Model** | Realizable k-ε Two-Layer |
| **Temporal Discretization** | $1^{st}$ order |
| **Iteration for Time Step** | 5 |
| **Maximum Courant Number per time-step** | 1 |
| **Gradient Discretization** | Hybrid Gauss-LSQ |
| **Algebraic system of Equations solver** | AGM - Algebraic Multigrid Solver |
| **Interface** | VoF - Volume of Fluid |
| **Convection Scheme for VoF** | HRIC - High-Resolution Interface Capturing |
| **Ship hull motion** | DBI - Dynamic Fluid Body Interaction |
| **Inner Iterations for DFBI** | 10 |
| **Mesh motion** | Overset Mesh |
| **Interpolation for Overset** | Linear |

The Background Volume is a block with a length of 8.5 times the *WTL*, a width of $3\cdot WTL$ and a height of 5·WTL m.

The boundary conditions are illustrated in Figure 15 (Background Region); the figure shows also the level of the water and the reference frame used during the simulation.

The -Y surface that closes the block (not represented) has a Symmetry boundary condition.

Figure 16 shows the boundary conditions applied to Overset Region, and in particular the Velocity Inlet boundary condition applied on the step surface to inject air.

The VoF Wave Model has been used to define the volume fraction, the magnitude and the direction of the velocity on the Velocity Inlet boundaries. Being the simulations in calm water, the selected VoF Wave Model is the Flat Wave.

The Flat Wave is the boundary condition imposed inside the numerical setup in order to simulate a state of calm sea without waves.

With this condition it is possible to fill with the water the background volume and the overset volume and to apply a constant velocity to the flow. The simulation results are relative to a navigation condition of the boat in calm water without waves. The study is conducted exclusively in calm water, as the air injection mechanism is unlikely to be activated in the presence of waves. Additionally, [50] has demonstrated that resistance reduction decreases under wave conditions.

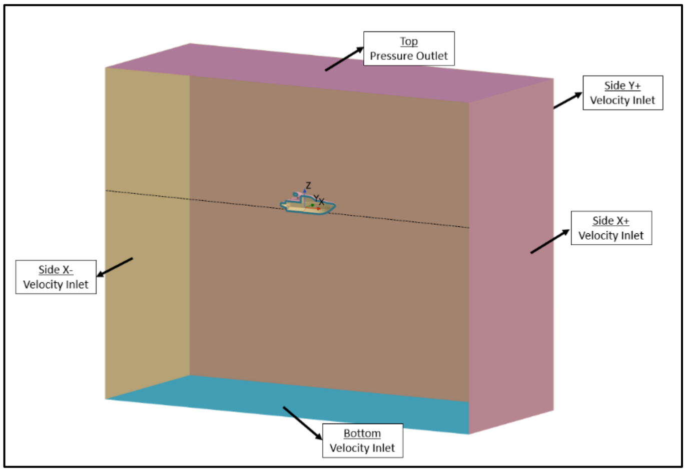

*Figure 15. Boundary conditions of the Background Volume*

The Overset Volume has been obtained offsetting the surface of the ship in the outer direction. The step is defined as a Velocity Inlet of only air and the velocity magnitude depends on the CQ value.

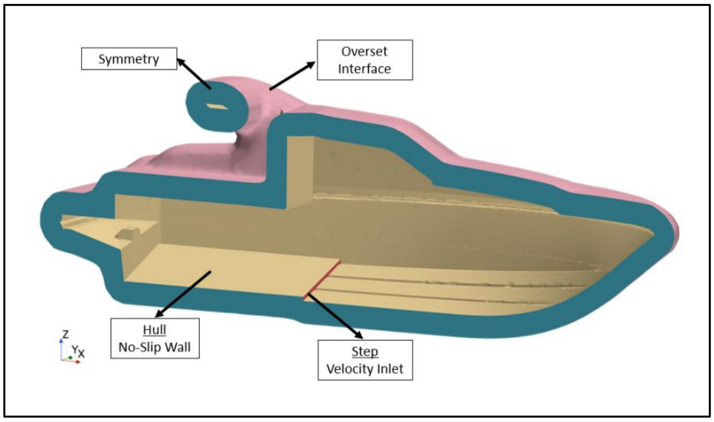

*Figure 16. Boundary conditions of the Overset Volume*

The mesh is a Trimmed Cell Mesh, with the base size being 3% of $BPX$ for the Overset Region. For the hull, the minimum surface cell size is 1.5% of $BPX$, while the mesh of the Background Region goes up to 63% of $BPX$. The minimum size for the Background goes down to 15% to refine the Interface and the volume around the Overset. The Overset mesh is displayed in Figure 17.

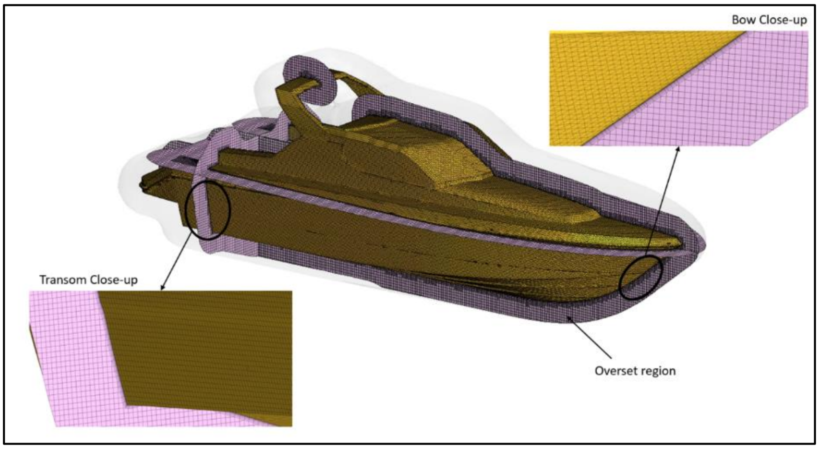

*Figure 17. Overset mesh*

## 3.5 Hull A simulations

The realized CFD simulations, both in full scale and in the tow tank scale, are reported in Table 8.

The velocity V is normalized with the Froude Number Fn (Eq. 4), while $Q_{air}$ refers to the mass airflow rate.

$$Fn = \frac{V}{\sqrt{g \cdot WTL}} \tag{4}$$

The total number of simulations in this first phase is 16.

*Table 8. Realized CFD simulation.*

| **1:6 Scale Simulations** | | | | | | | | |
|---|---|---|---|---|---|---|---|---|
| **Simulation** | 1 | 2 | 3 | 4 | 5 | 6 | 7 | 8 |
| **Fn** | 0.51 | 0.8 | 1 | 1.4 | 0.51 | 0.77 | 1.02 | 1.36 |
| **$Q_{air}$ [l/min]** | 0 | 0 | 0 | 0 | 8500 | 8500 | 8500 | 8500 |
| **Full-scale Simulations** | | | | | | | | |
| **Simulation** | 9 | 10 | 11 | 12 | 13 | 14 | 15 | 16 |
| **Fn** | 0.51 | 0.8 | 1 | 1.4 | 0.51 | 0.77 | 1.02 | 1.36 |
| **$Q_{air}$ [l/min]** | 0 | 0 | 0 | 0 | 8500 | 8500 | 8500 | 8500 |

## 3.6 Hull B simulations

A speed range was defined to properly characterize the hull, starting from a non-planing condition and gradually reaching the intended planing condition. Initially, a comparison was made between the performance of the original (baseline) hull and the hull with the step in the absence of air cavities. After confirming that the total resistance and trim remained largely unchanged, especially within the operating range, a simulation campaign was initiated to test the hull with the step at five different speeds. The simulation with air injection are also categorized by the Flow Rate Coefficient (CQ). CQ is defined as the ratio between the injected air velocity and the hull velocity. The campaign of simulation is reported in Table 9.

*Table 9. Tests on baseline hull and stepped hull*

| | **ID** | **$V_H$ [kn]** | **$V_H$ [m/s]** | **CQ** | **$V_A$ [m/s]** | **Fn** |
|---|---|---|---|---|---|---|
| **Baseline design** | **12_BL** | 12 | 6.17 | - | - | 0.55 |
| | **18_BL** | 18 | 9.26 | - | - | 0.82 |
| | **24_BL** | 24 | 12.35 | - | - | 1.09 |
| | **30_BL** | 30 | 15.43 | - | - | 1.37 |
| | **36_BL** | 36 | 18.52 | - | - | 1.64 |
| **Stepped hull, no air injection** | **12_0** | 12 | 6.17 | - | - | 0.55 |
| | **18_0** | 18 | 9.26 | - | - | 0.82 |
| | **24_0** | 24 | 12.35 | - | - | 1.09 |
| | **30_0** | 30 | 15.43 | - | - | 1.37 |
| | **36_0** | 36 | 18.52 | - | - | 1.64 |
| **Stepped hull with air injection** | **12_1** | 12 | 6.17 | 1 | 6.17 | 0.55 |
| | **12_2** | 12 | 6.17 | 2 | 12.34 | 0.55 |
| | **12_3** | 12 | 6.17 | 3 | 18.51 | 0.55 |
| | **18_1** | 18 | 9.26 | 1 | 9.26 | 0.82 |
| | **18_2** | 18 | 9.26 | 2 | 18.52 | 0.82 |
| | **18_3** | 18 | 9.26 | 3 | 27.78 | 0.82 |
| | **24_1** | 24 | 12.35 | 1 | 12.35 | 1.09 |
| | **24_2** | 24 | 12.35 | 2 | 24.7 | 1.09 |
| | **24_3** | 24 | 12.35 | 3 | 37.05 | 1.09 |
| | **30_1** | 30 | 15.43 | 1 | 15.43 | 1.37 |
| | **30_2** | 30 | 15.43 | 2 | 30.86 | 1.37 |
| | **30_3** | 30 | 15.43 | 3 | 46.29 | 1.37 |
| | **36_1** | 36 | 18.52 | 1 | 18.52 | 1.64 |
| | **36_2** | 36 | 18.52 | 2 | 37.04 | 1.64 |
| | **36_3** | 36 | 18.52 | 3 | 55.56 | 1.64 |

In the simulation with air injection, three different air speeds were tested for each hull speed. Once the simulations were completed, a Java macro was developed to be executed within the Simcenter STAR-CCM+ environment to extract the volumes of air cavities beneath the hull for each tested condition. The volumes are processed in MeshLab to obtain the main geometrical characteristics and the data from the CFD simulation and the volume analysis is then processed in Matlab.

### 3.6.1 Macro for volume and mass flow rate extraction

The Java macro performs several operations to extract the air volume under the hull and the values of the mass flow rates. Firstly, it isolates, from the entire fluid region, only the portion with an air volume fraction between 0.5 and 1. Once this portion of the volume is isolated, the macro performs a Boolean intersection between the obtained volume and a known-sized block (Air Control Volume) positioned beneath the hull, between the step and the transom. The Boolean intersection is then exported in STL format and the air volume is therefore obtained.

To extract the values of mass flow rates, three surfaces are defined as in Figure 18. The macro then creates three reports of Air Mass Flow Rate (one for each surface) and the results are written to an output file.

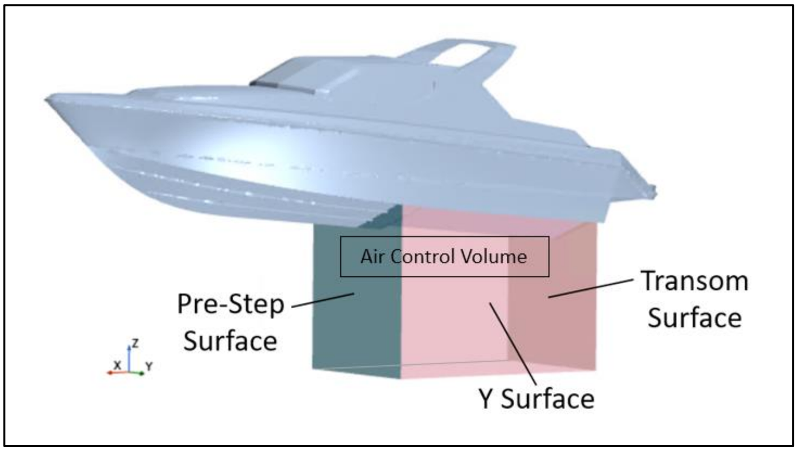

*Figure 18. Surfaces of the control volume*

### 3.6.2 Volume analysis in Meshlab

The Metro tool [51] utilizes Hausdorff's method to calculate distances between points and surfaces. The distance between a point p and a surface S, denoted as e(p, S), is defined as the minimum Euclidean distance between p and any point $p_0$ on S (Eq. 5).

$$e(p,S) = \min\big(d(p,p')\big)\,, p' \epsilon S \tag{5}$$

To determine the distance between two surfaces, $S_1$ and $S_2$, the tool calculates E(S1, S2) as the maximum distance between any point in $S_1$ and surface $S_2$. Afterwards, the tool assigns a coefficient, w(X, Y, Z), to each distance, ranging from 0 to 1, and maps it to an RGB color scale using a piecewise linear transfer function. The color gradient transitions from red to blue as the distance between the air layer on the hull and the bottom part of the air volume increases. The coefficient w(X, Y, Z) represents a dimensionless wear value, which can be converted to the actual wear, W(X, Y, Z), by measuring the maximum distance between the two surfaces (when w(X, Y, Z) equals 1).

### 3.6.3 Air Dissipation Ratio coefficient

To account for the variation of the distribution of the air under the hull in different operating conditions, the Air Direction Ratio (ADR) was introduced and it was defined as the ratio between the air flowing through the side of the hull and the air flowing through the transom surface (Eq. 6).

$$ADR = \frac{Q_T}{Q_Y} \tag{6}$$

$Q_T$ is the flow rate through the Transom Surface in Figure 18, while $Q_Y$ is the flow rate through the Y Surface in Figure 18.

The ADR parameter is essential to capture how the air layer spatial distribution changes with different speeds and CQ values, providing valuable insights into the overall air trapping characteristics beneath the hull.

When the value is less than 1, it means that the air layer is developed towards the chine; when the value is greater than 1, the air layer is developed towards the transom, so the air escapes from behind the hull without branching out towards the chine on the left and on the right.

Figure 41 shows an instance of the behaviour of the airflow for ADR<1 and ADR>1. The ADR<1 instance is from the simulation with Fn 0.82 and CQ=1: in this case the airflow introduced from the step deviates towards the chine and escapes laterally.

The ADR>1 instance is from the simulation with Fn 1.64 and CQ=3: the airflow is now directed towards the transom, with almost no lateral escape.

### 3.6.4 Spray Rails Airflow Fraction

Another parameter defined is the Spray Rails Airflow Fraction (SRAF). This value has been defined to check how much of the airflow under the hull is transported by the spray rails and how much is introduced from the air injection (Eq. 7).

$$SRAF = \frac{Q_{PS}}{Q_T + Q_Y} \tag{7}$$

$Q_T$ and $Q_Y$ were already defined in the section 3.6.3; $Q_{PS}$ is the flow rate through the Pre-Step Surface in Figure 18.

### 3.6.5 Simulations with propellers

The CFD setup of the hull with propellers is the same as the one defined in §3.4. To model the propellers, two additional cylindric regions were created inside the Overset Volume, thus generating two interfaces. Inside each region, a propeller was placed.

To simulate the effect of rotating blades, the propellers (modelled as Walls) were kept fixed, while in their region two Moving Reference Frames (MRFs) were defined. The origins of the MRFs are placed on the centre of rotation of the propeller and the rotation rate is defined in order to obtain the desired advance velocity of the ship. The regions of the propellers are included in the DFBI model, so both the centre of rotation and the rotation axis are updated during the simulation following the heave, trim and advance of the ship. The studied propeller is the INSEAN E779A, which has been scaled to be applied to the hull under examination. The characteristics of the propeller are listed in Table 10 and it is represented in Figure 19.

*Table 10. Propeller dimensions*

| **Propeller characteristics** | |
|---|---|
| Propeller diameter | 380 mm |
| Number of blades | 4 |
| Hub diameter | 130 mm |
| Hub length | 140 mm |

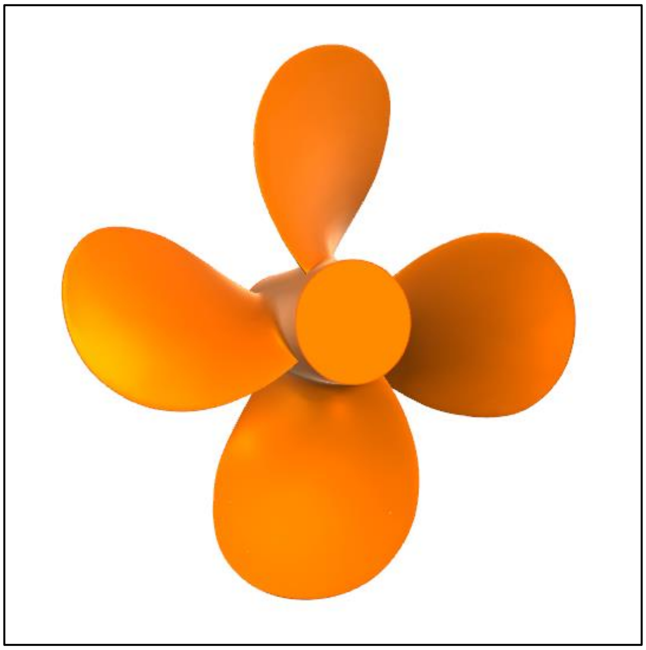

*Figure 19. Propeller geometry*

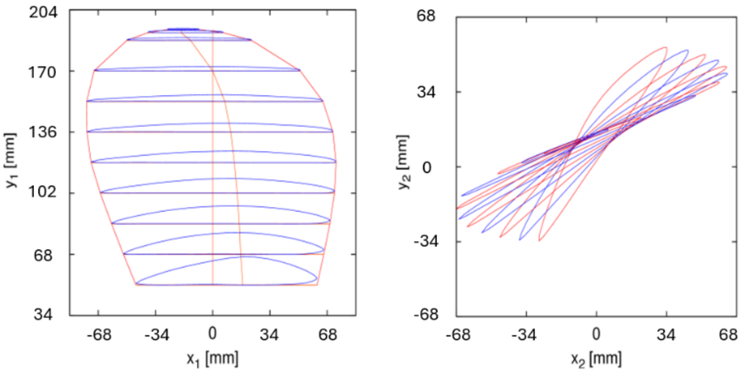

*Figure 20. Propeller sections*

Four propellers have been installed as shown in Figure 21.

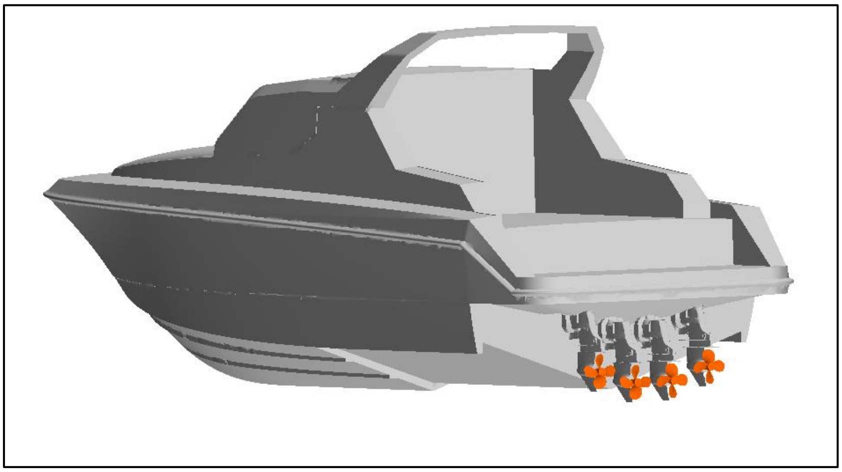

*Figure 21. Propellers installations on the hull*

# 4. Results and Discussion

## 4.1 Hull A

The hull A has been used to validate the CFD model and investigate the scalability of the air distribution under the hull. The results were organized in two different sub-paragraphs: 4.1.1 and 4.1.2.

### 4.1.1 CFD model validation

The results of the CFD simulations were organized from Figure 22 to Figure 25, in order to evaluate the resistance trends obtained both at 1:6 scale and at full scale, respectively compared with the results of the towing tank tests and those scaled using ITTC.

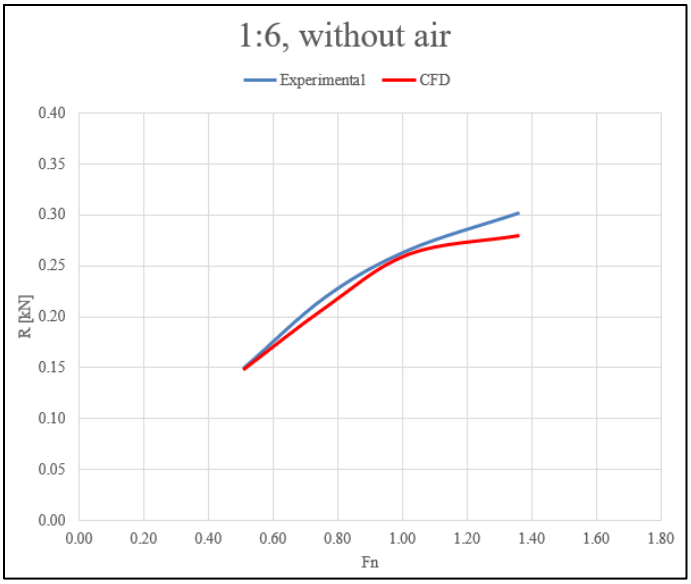

*Figure 22. CFD vs experimental, 1:6 scale without air injection*

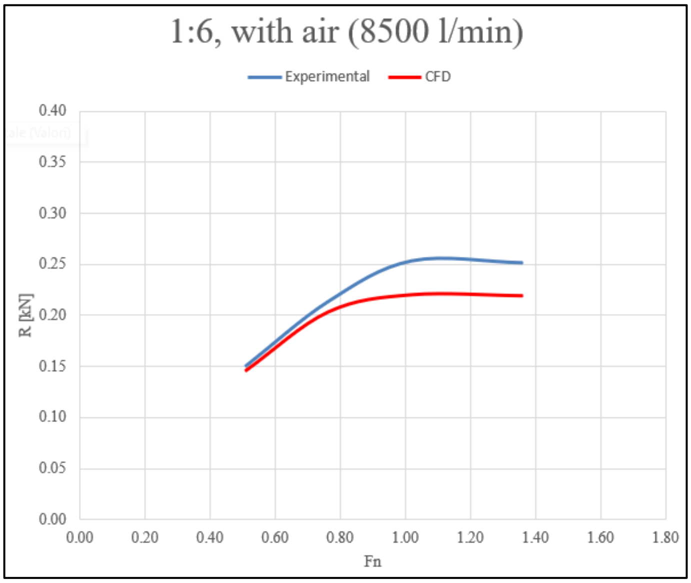

*Figure 23. CFD vs experimental, 1:6 scale with air injection*

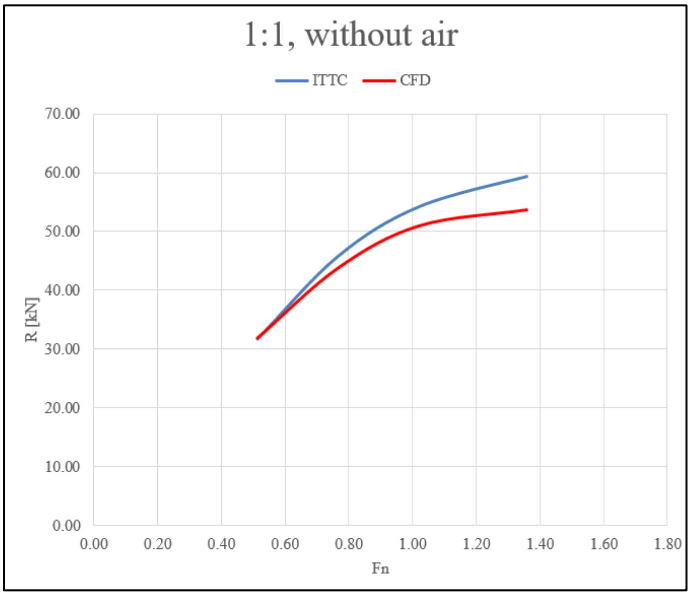

*Figure 24. CFD vs ITTC, 1:1 scale without air injection*

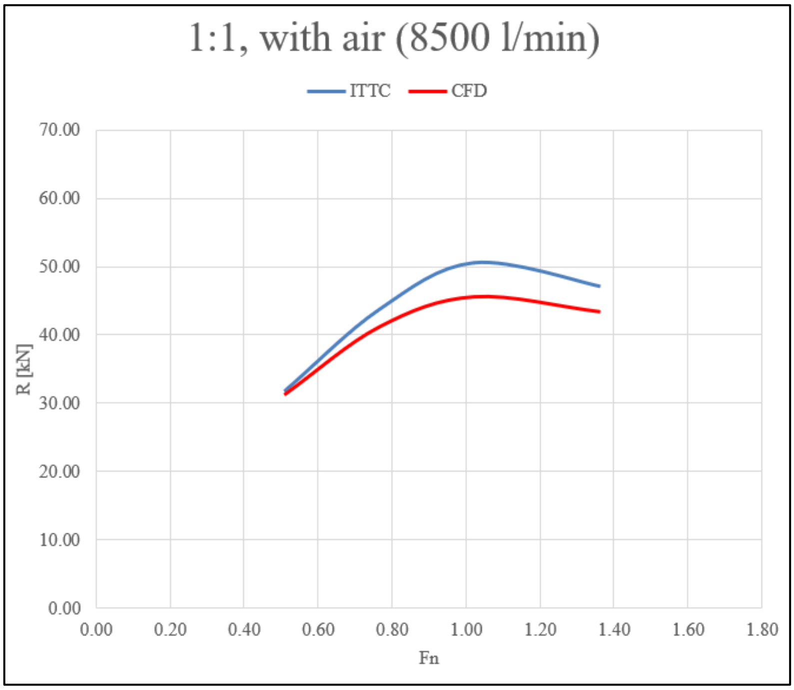

*Figure 25. CFD vs ITTC, 1:1 scale with air injection*

The trend of the resistance in absence of air injection is well-captured both for the full scale and scaled models.

The differences between the numerical results and the experimental/ITTC ones are calculated in Table 11.

The differences are acceptable for all the simulated conditions, so the model has been considered correlated.

*Table 11. Hull A simulations, difference evaluation*

| Simulation | Fn | % diff. (CFD vs EXP/ITTC) |
|---|---|---|
| 1:6, without air injection | 0.511 | 1.333 |
| | 0.766 | 5.001 |
| | 1.022 | 1.880 |
| | 1.362 | 7.615 |
| 1:6, with air injection | 0.511 | 2.667 |
| | 0.766 | 5.140 |
| | 1.022 | 13.386 |
| | 1.362 | 13.095 |
| 1:1, without air injection | 0.511 | 0.351 |
| | 0.766 | 4.512 |
| | 1.022 | 6.156 |
| | 1.362 | 9.697 |
| 1:1, with air injection | 0.511 | 1.852 |
| | 0.766 | 5.911 |
| | 1.022 | 9.889 |
| | 1.362 | 7.953 |

### 4.1.2 Air distribution evaluation

From Figure 26 to Figure 28, images that combine air volume fraction maps in the upper half and air streamlines originating from the step in the lower half are shown.

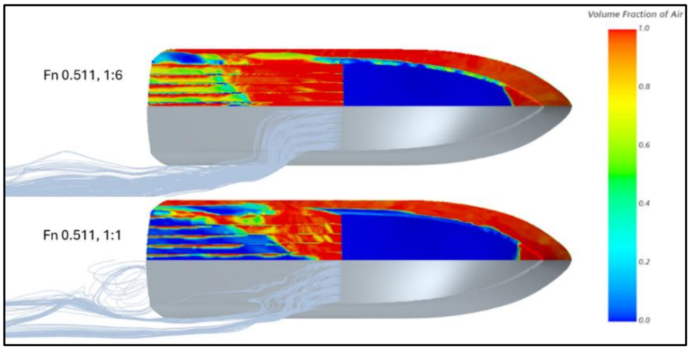

*Figure 26. Hull ventilation at Fn 0.511*

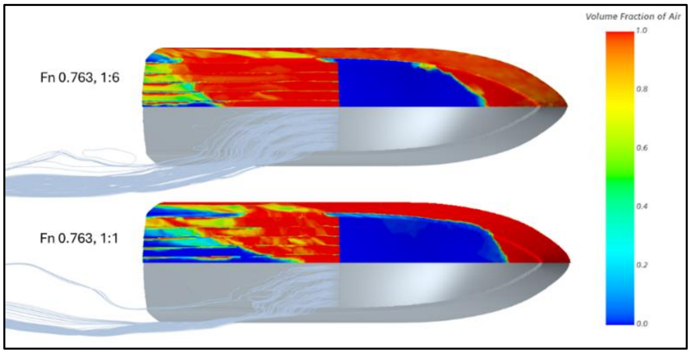

*Figure 27. Hull ventilation comparison at Fn 0.763*

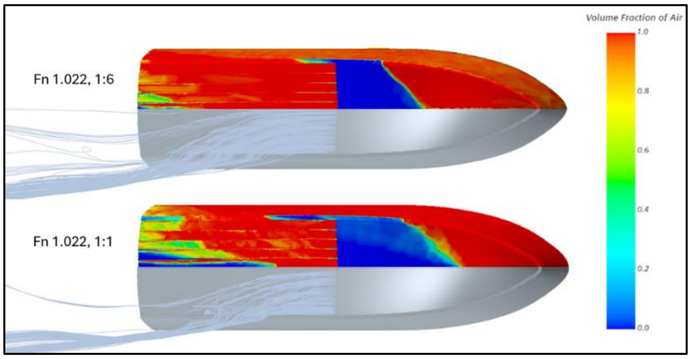

*Figure 28. Hull ventilation comparison at Fn 1.022*

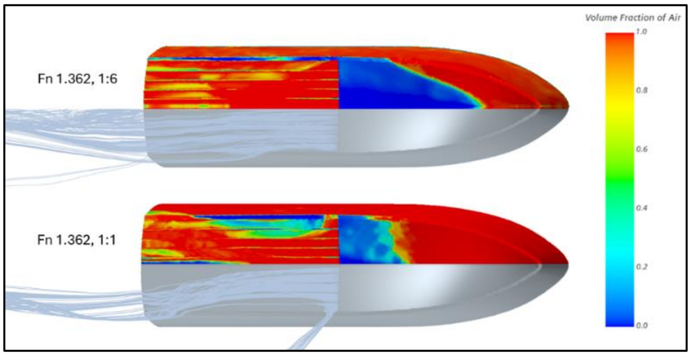

*Figure 29. Hull ventilation comparison at Fn 1.362*

It can be observed that the airflow emitted from the step remains more compact in the 1:6 scale simulations compared to the 1:1 scale, making the scaled model overall more ventilated. This difference gradually decreases as the Froude number increases. The increase in the Froude number, along with the proportional rise in the Reynolds number, leads to an increase in turbulence, which enhances air-water mixing, making the airflow less cohesive even in the 1:6 scale case, under both pre-planing and planing conditions.

The 1:1 simulations show a higher air dispersion at all the considered Froude numbers.

This is due to two important aspects:

- changes in surface tension due to length scale difference between model and ship;
- changes in inertial forces due to velocity differences between 1:6 and 1:1 simulations.

Among the dimensionless groups commonly used in the literature to define problems of this type, the Bond number (Eq. 8) is not considered.

$$Bo = \frac{\Delta\rho \cdot WTL^2 \cdot g}{\sigma} \propto \lambda^2 \tag{8}$$

The Bond number expresses the relationship between surface tension forces and gravitational forces. Unlike the Froude and Reynolds numbers (Eq. 9 and Eq. 10), it is independent of velocity, making it important for distinguishing pure scaling effects from those related to differences in velocity.

$$Fn = \frac{V}{\sqrt{g \cdot WTL}} \propto \lambda^{1/2} \tag{9}$$

$$Re = \frac{\rho \cdot WTL \cdot V}{\mu} \propto \lambda^{3/2} \tag{10}$$

Moreover, the Bond number is the one that shows the bigger dependence from the scale factor $\lambda$.

The three numbers have been calculated for each condition.

*Table 12. Calculations for 1:6 simulations*

| **λ** | **Fn** | **Bo** | **Re** |
|---|---|---|---|
| 1/6 | 0.511 | $8.354 \cdot 10^5$ | $7.044 \cdot 10^6$ |
| 1/6 | 0.766 | $8.354 \cdot 10^5$ | $1.051 \cdot 10^7$ |
| 1/6 | 1.022 | $8.354 \cdot 10^5$ | $1.401 \cdot 10^7$ |
| 1/6 | 1.362 | $8.354 \cdot 10^5$ | $1.861 \cdot 10^7$ |

*Table 13. Calculations for 1:1 simulations*

| **λ** | **Fn** | **Bo** | **Re** |
|---|---|---|---|
| 1 | 0.511 | $3.007 \cdot 10^7$ | $1.029 \cdot 10^8$ |
| 1 | 0.766 | $3.007 \cdot 10^7$ | $1.543 \cdot 10^8$ |
| 1 | 1.022 | $3.007 \cdot 10^7$ | $2.058 \cdot 10^8$ |
| 1 | 1.362 | $3.007 \cdot 10^7$ | $2.744 \cdot 10^8$ |

The Bond number is significantly lower in the 1:6 case. When the Bond number is low, it means that the surface tension effects are predominant on the gravitational forces. A high surface tension hinders air-water mixing, so the airflow vein coming from the step stays coherent and does not branch out towards the chine like in the 1:1 simulation. This effect becomes less important with the increase of the Reynolds number, which facilitates phase mixing due to turbulence: this explains why in planing conditions also the airflow in the 1:6 model branches out towards the chine.

## 4.2 Hull B

Starting from the validated CFD model, hull B has been characterised without and with the step. Different simulations were made to study its hydrodynamic behaviour under different air injection conditions. Scaled INSEAN E779A propellers were also added in the model to study the hull-propellers interaction.

### 4.2.1 Definition of the step position

The baseline hull, as previously mentioned, lacks a step. To facilitate air injection, a step must be incorporated beneath the hull. Unlike typical planing hull designs, where steps are often used to create natural ventilation along the sides, the placement of this step is not driven by that principle. The primary objective at this stage is to ensure the step remains fully submerged under all operating conditions of the boat. Keeping the step submerged prevents the injected air from dissipating directly into the atmosphere. To determine the optimal position for the step, an initial simulation was performed, focusing on locating a suitable air inlet point. The step must always be submerged to maximize the effectiveness of the air injection. To find the correct placement, a simulation of the baseline hull at a Froude number (Fn) of 1.64, corresponding to its maximum design speed, was conducted. This scenario also represents the condition with the least wetted surface area. The results (Figure 30) indicate that, in its equilibrium state, the hull remains submerged for 4.4 meters from the transom (LST=4.4 meters).

Therefore, the step was positioned at this distance, as it is essential to inject air into a consistently submerged area to fully harness the benefits of air injection. Along the hull centreline, no air is trapped by numerical ventilation.

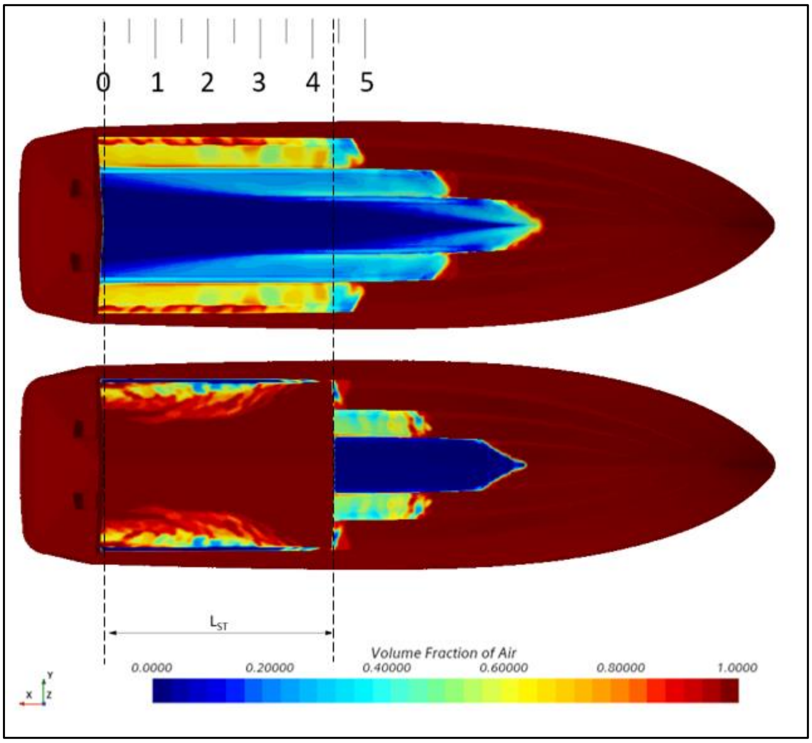

*Figure 30. Comparison between baseline and stepped hull at Fn 1.64 with CQ3*

### 4.2.2 Comparison between baseline and stepped hull

The baseline hull and the stepped hull without air injection were tested at the velocities listed in Table 9.

The simulation results are presented in Table 14.

The hull resistance has been reported after normalizing it with the displacement Δ.

*Table 14. Results from simulations on baseline and stepped hull without air injection*

| **Fn** | **Hull Resistance Normalized with Displacement** | | **Trim [deg]** | |
|---|---|---|---|---|
| | **BL** | **0** | **BL** | **0** |
| **0.55** | 0.135 | 0.144 | 5.5 | 5.5 |
| **0.82** | 0.155 | 0.159 | 6.5 | 6.6 |
| **1.09** | 0.157 | 0.155 | 6.7 | 6.7 |
| **1.37** | 0.143 | 0.131 | 5.4 | 5.2 |
| **1.64** | 0.137 | 0.117 | 4.3 | 4.2 |

The total hull resistance shows a slight increase in the stepped design at Froude numbers (Fn) below 1, while it decreases for Fn values above 1. At Fn 1.64, the hull resistance of the stepped design is 85% of that of the baseline hull. Additionally, the trim angle of the boat remains virtually unchanged in the stepped version, whereas the wetted surface area is reduced across all tested speeds. These results suggest that the introduction of the step did not degrade performance. The trim angle remains nearly constant, and although hull resistance increases slightly in the non-planing region, it decreases in the planing region, which is the primary operational condition of interest. Consequently, the stepped hull can now be studied with air injection. After verifying that the modification did not negatively impact the vessel's performance, simulations with air injection were conducted. The simulations were performed, and the results related to the main hydrodynamic quantities are presented in Table 15, including the normalized wet area $S_{w,n}$ (Eq.11).

$$S_{w,n} = \frac{S_w}{S_w + S_v} \tag{11}$$

$S_w$ is the wet area and $S_v$ is the ventilated area: both are extracted from the CFD simulations for every Fn and every CQ.

The complement to 1 of $S_{w,n}$ represents the normalized ventilated area $S_{v,n}$.

*Table 15. Results from simulations on stepped hull with air injection*

| **Fn** | **Hull Resistance Normalized with Displacement** | | | **Trim [deg]** | | | **Normalized Wet Area** | | |
|---|---|---|---|---|---|---|---|---|---|
| | **CQ1** | **CQ2** | **CQ3** | **CQ1** | **CQ2** | **CQ3** | **CQ1** | **CQ2** | **CQ3** |
| **0.55** | 0.143 | 0.142 | 0.140 | 5.5 | 5.5 | 5.5 | 0.830 | 0.808 | 0.828 |
| **0.82** | 0.166 | 0.168 | 0.174 | 7.1 | 7.4 | 7.9 | 0.641 | 0.579 | 0.559 |
| **1.09** | 0.154 | 0.157 | 0.157 | 6.8 | 7.3 | 7.5 | 0.413 | 0.367 | 0.363 |
| **1.37** | 0.128 | 0.124 | 0.120 | 5.2 | 5.1 | 4.9 | 0.342 | 0.342 | 0.334 |
| **1.64** | 0.109 | 0.105 | 0.104 | 3.8 | 3.7 | 3.7 | 0.265 | 0.261 | 0.257 |

The results collected in Table 14 and Table 15 have been represented in graphs from Figure 31 to Figure 33. For each graph, the examined quantity is plotted against the Froude number of the hull, with each curve parameterized according to the value of CQ.

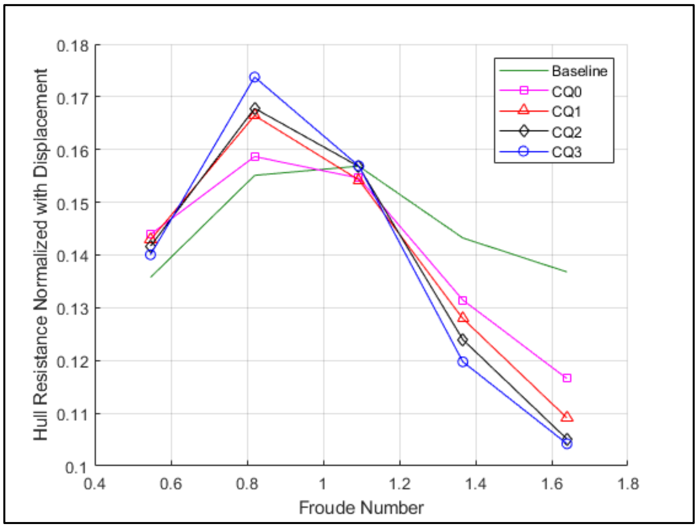

*Figure 31. Hull resistance at different hull and air velocities*

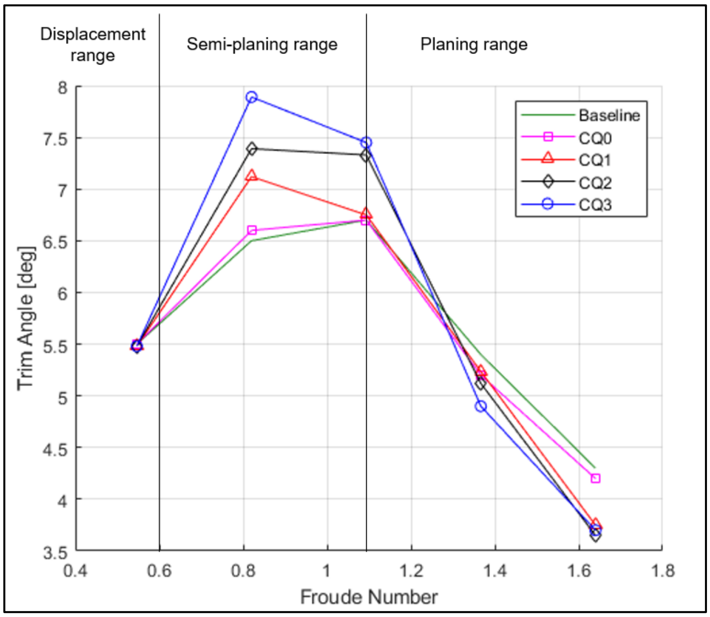

*Figure 32. Trim angle at different hull and air velocities*

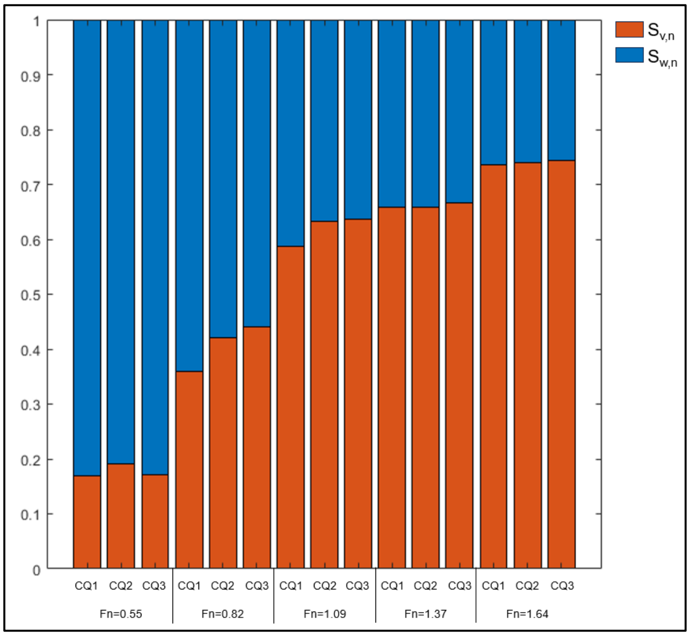

*Figure 33. bar plot of normalized wet and ventilated area*

In Figure 31, the trend of hull resistance for different velocities is shown. Below a Froude number of 1.09, an increase in air ventilation velocity leads to a rise in total resistance because the reduction in wetted surface area does not offset the increase in pressure resistance caused by the higher trim angle. However, above Fn 1.09, this trend reverses, and resistance decreases as the CQ value increases. From Figure 32, it is evident that at higher air velocities, the trim angle values increase up to Fn 1.09 (therefore still in semi-planing conditions). However, above Fn 1.09, as the air velocity increases, the trim angle decreases.

Considering Figure 33, it can be observed that the wetted surface area decreases as the Froude number increases. For Fn

0.55, there is not a clear change in wetted area as the CQ increases. The hull dries evidently with the increasing of CQ for Fn 0.82 and Fn 1.09 and then the effect of CQ becomes again less influent for higher Froude number.

For greater clarity, using the data in Table 14 and Table 15, the trend of the relative change in hull resistance with respect to the baseline design has been calculated and it’s reported in Figure 34. The plot once again highlights how the greatest benefits are obtained under planing conditions, with the hull resistance going down to the 76% of the baseline value at 36 kn for CQ3.

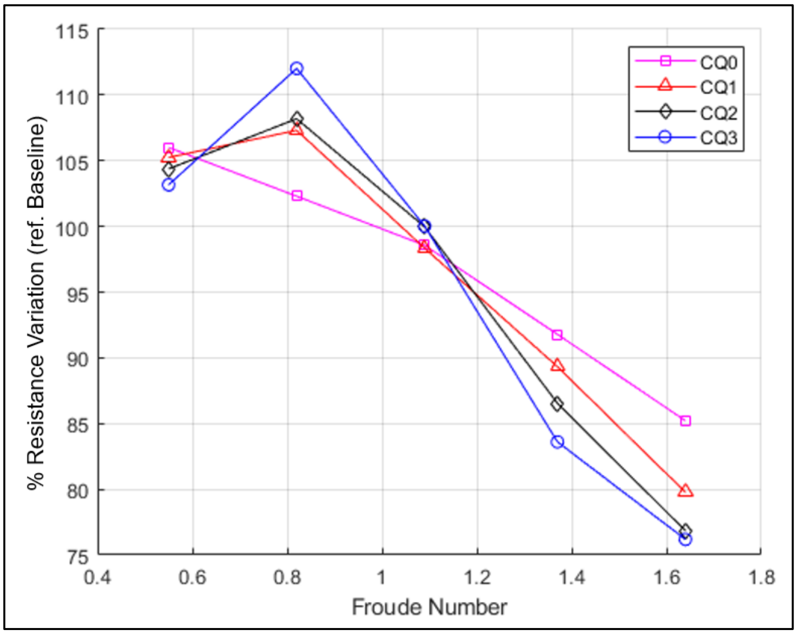

*Figure 34. percentage of hull resistance change referred to the baseline design*

The analysis reveals that Fn 1.09 can be regarded as a critical speed, marking the transition between non-planing and planing conditions. For speeds above Fn 1.09 but below Fn 1.37 (the hull's operating range), it is not beneficial to consider CQ values greater than 2 when aiming to reduce total resistance. Beyond this point, increasing the air velocity does not result in a significant reduction in hull resistance. Results related to sinkage for each Froude number and each CQ were also extracted from the CFD simulations.

The sinkage has been normalized dividing it by the draft *DFT*: the normalized values are reported in Table 16.

*Table 16. Normalized sinkage*

| | **Sinkage Normalized with Draft** | | | | |
|---|---|---|---|---|---|
| | **BL** | **CQ0** | **CQ1** | **CQ2** | **CQ3** |
| **0.55** | -0.036 | -0.050 | -0.043 | -0.050 | -0.042 |
| **0.82** | 0.223 | 0.224 | 0.237 | 0.250 | 0.276 |
| **1.09** | 0.488 | 0.487 | 0.513 | 0.566 | 0.592 |
| **1.37** | 0.619 | 0.618 | 0.671 | 0.697 | 0.724 |
| **1.64** | 0.712 | 0.711 | 0.724 | 0.737 | 0.750 |

### 4.2.3 Geometric assessment of the air layer

This paragraph presents the results obtained from the analysis conducted on MeshLab on the volumes of air.

Figure 35, Figure 36 and Figure 37 show contour plots that display, for each CQ condition and varying hull velocity, a map depicting in the lower half of the hull the local normalized thickness of the air layer trapped beneath the hull. To enhance the visualization of the phenomenon, a Volume Fraction of Water contour has been represented on the upper half of the hull.

Unlike the traditional area-based representation, which only shows where the wet and ventilated areas are located, this new system allows for the visualization of the local thicknesses of the air layer.

This is particularly valuable as it reveals the effects associated with the presence of spray rails and the lateral air flow escape phenomenon.

To normalize the air layer thickness, a mean boundary layer height δ has been calculated.

This calculation is based on the Reynolds number: a mean value of the tested velocities has been considered to obtain a mean Reynolds number, considering as characteristic length *LH*, which was already used in the Froude number calculation.

After obtaining the Reynolds number corresponding to the mean of the tested hull velocities, δ has been calculated as in Eq. 12 considering a turbulent flow [52].

$$\delta = 0.37 \cdot LH \cdot Re^{-1/5} = 0.11\,m \qquad (12)$$

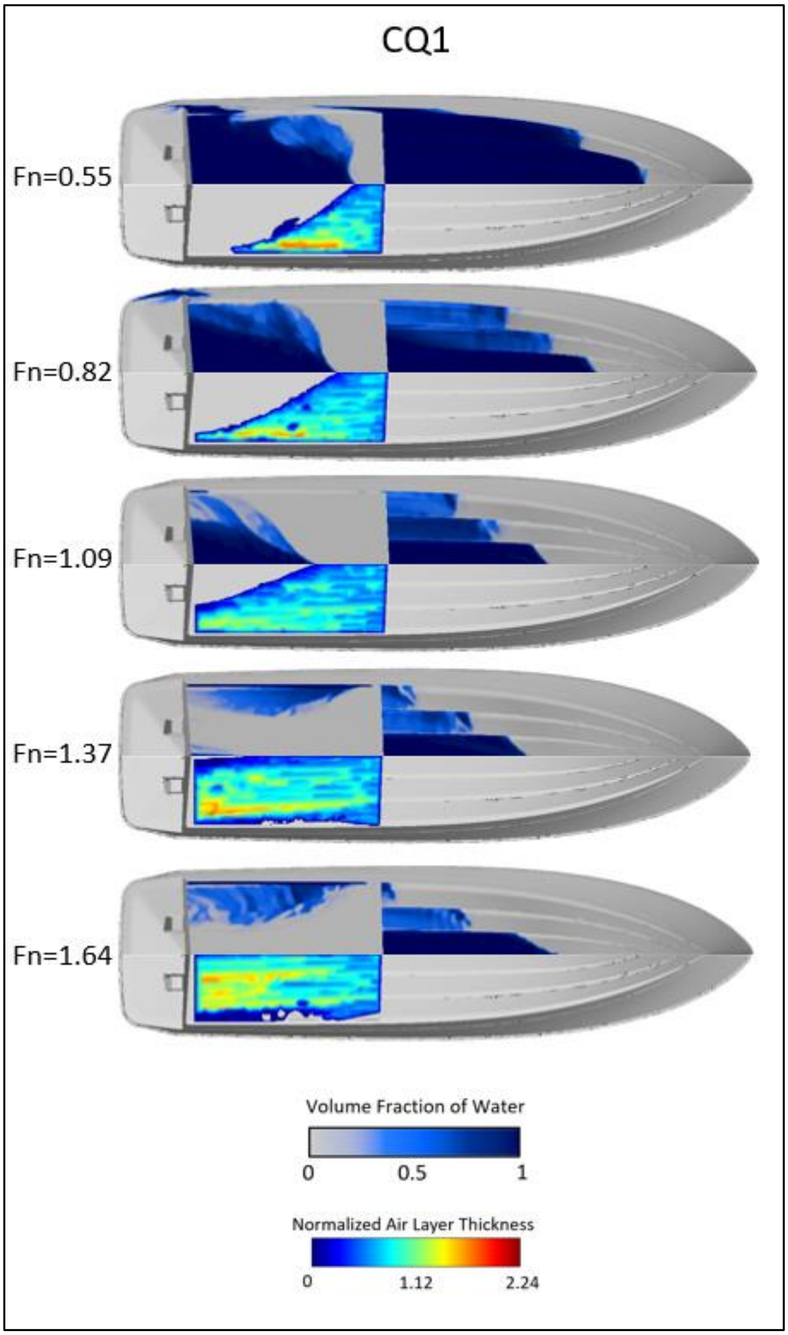

*Figure 35. Air Layer Thickness and Volume Fraction of Water contour plot for CQ1*

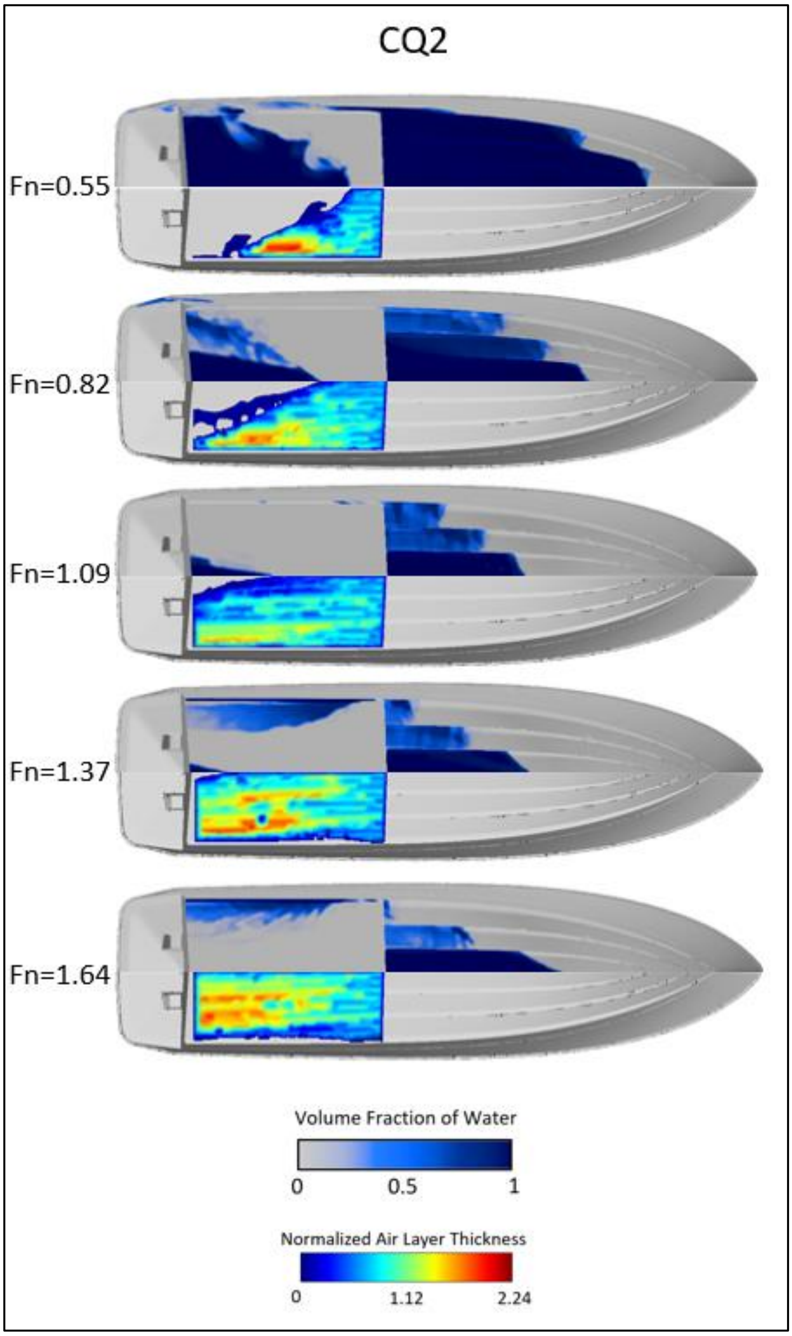

*Figure 36. Air Layer Thickness and Volume Fraction of Water contour plot for CQ2*

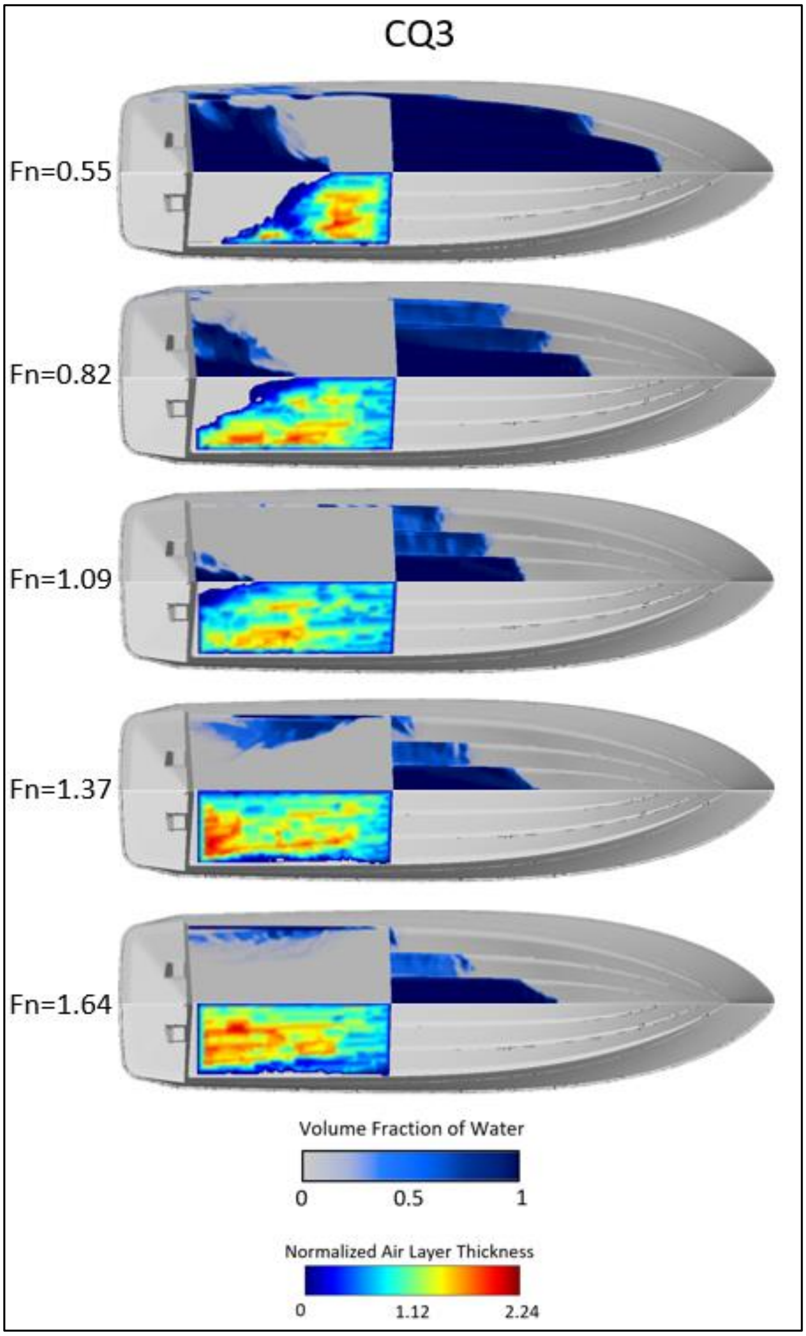

*Figure 37. Air Layer Thickness and Volume Fraction of Water contour plot for CQ3*

For each CQ condition, the color bar scale remains fixed. As CQ increases and the hull velocity remains constant, the air trapped beneath the hull fills the Air Control Volume (defined in Figure 18) more extensive, so both the Mean and Maximum air thickness increase as a result.

The numerical values of both the Normalized Mean and Maximum Air Layer Thickness calculated for every condition by the Metro tool in MeshLab are reported in Table 17 and Table 18. The values are plotted in Figure 38 and Figure 39.

*Table 17. Maximum Air Layer Thickness for every motion condition*

| **Fn** | **Normalized Maximum Air Layer Thickness for** | | |
|---|---|---|---|
| | **CQ1** | **CQ2** | **CQ3** |
| **0.55** | 1.77 | 1.96 | 2.03 |
| **0.82** | 1.68 | 1.84 | 1.94 |
| **1.09** | 1.47 | 1.57 | 1.82 |
| **1.37** | 1.75 | 2.03 | 2.16 |
| **1.64** | 1.65 | 1.87 | 2.03 |

*Table 18. Mean Air Layer Thickness for every motion condition*

| **Fn** | **Normalized Mean Air Layer Thickness for** | | |
|---|---|---|---|
| | **CQ1** | **CQ2** | **CQ3** |
| **0.55** | 0.37 | 0.41 | 0.47 |
| **0.82** | 0.41 | 0.47 | 0.56 |
| **1.09** | 0.44 | 0.47 | 0.58 |
| **1.37** | 0.40 | 0.47 | 0.53 |
| **1.64** | 0.38 | 0.50 | 0.52 |

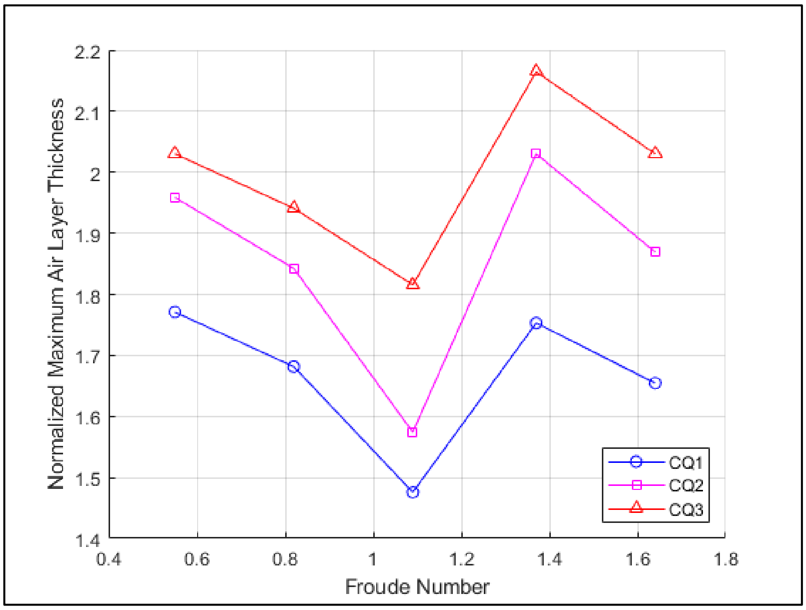

*Figure 38. Maximum Air Layer Thickness plot*

From Figure 38, it is evident that the maximum thickness of the air layer decreases with a decrease in CQ. Additionally, for the same CQ, the maximum thickness value shows different trends under different hull speed conditions. The maximum air layer thickness decreases going towards higher hull speeds in non-planing conditions, and it increases between Fn 1.09 and 1.37. As the hull speed continues to increase beyond Fn 1.37, the maximum air layer thickness starts decreasing again.

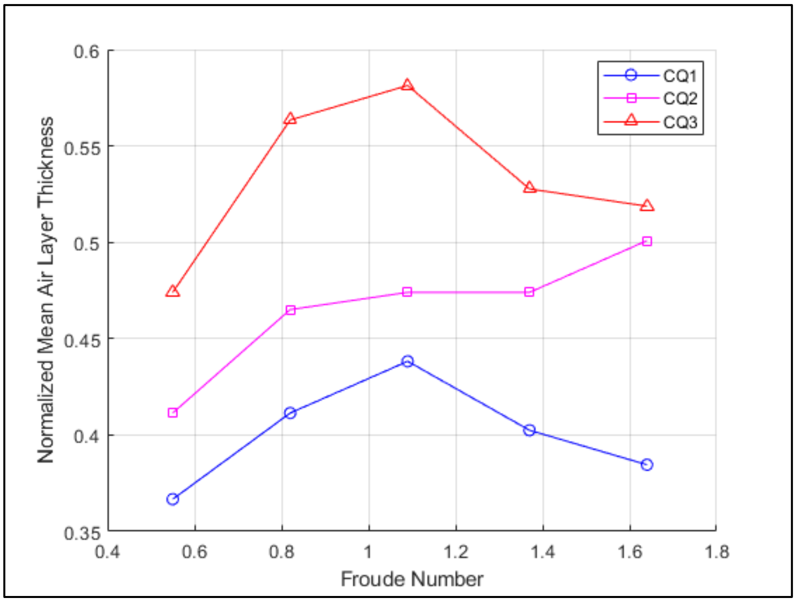

*Figure 39. Mean Air Layer Thickness plot*

From the plot of Mean Air Layer Thickness in Figure 39, in non-planing conditions, the Mean air layer thickness increases for every CQ.

As the hull velocity increases above Fn 1.09, the airflow tends to distribute more evenly across the step, resulting in a reduction in the average thickness. This effect has been observed as expected for both CQ1 and CQ3. However, it appears to deviate from the expected behaviour for CQ2, where the cushion tends to increase in thickness: this is because, at that flow rate, complete step filling occurs at a higher velocity (see Figure 36).

In Figure 40, Normalized Resistance Variation for CQ1, CQ2 and CQ3 calculated as $\frac{R-R(CQ0)}{R}$

was plotted as a function of Normalized Ventilated Area and of Normalized Mean Air Layer Thickness.

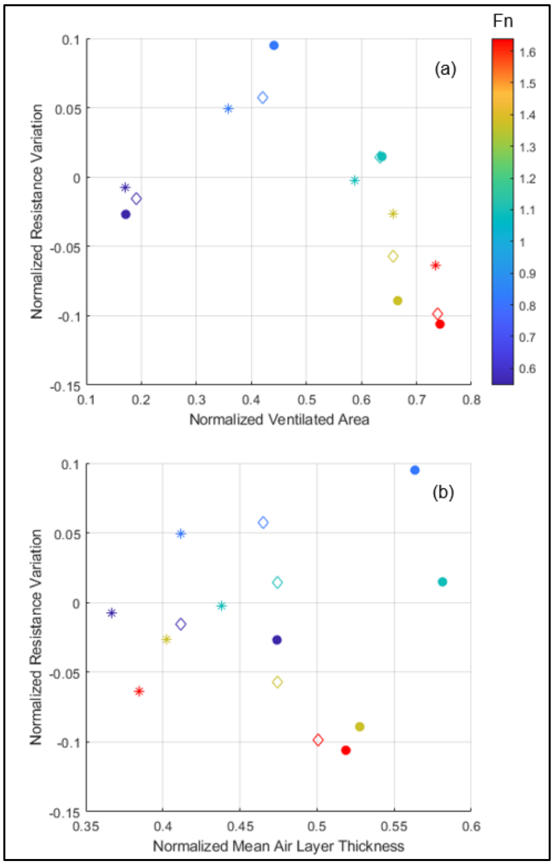

*Figure 40. Scatter plot for Normalized Resistance Variation against Normalized Ventilated area (a) and Normalized Mean Air Layer Thickness (b).*

Figure 40a confirms that going towards higher Fn, as expected, leads to an increase of $S_{v,n}$. In the planing region, a higher $S_{v,n}$ corresponds to a lower hull resistance, but the trend reverses in the semi-planing and displacement regions. A parabolic trend of the resistance can be discerned: the Normalized Resistance Variation values are between 0 and -0.05 at Fn 0.55, then they reach higher values at Fn 0.82 and then they decrease until Fn 1.64.

Figure 40b shows that a higher Mean Air Layer thickness leads to a greater resistance reduction only for Fn 0.55, Fn 1.37 and Fn 1.64.

In the semi-planing region a higher mean air layer thickness does not correspond to a resistance reduction.

Analysing the plots of Mean and Maximum thickness it becomes apparent that the distribution of the air layer changes with hull speed and CQ values. To account for this, the Air Direction Ratio (ADR) was introduced.

Figure 41 shows an instance of the behaviour of the airflow for ADR<1 and ADR>1. The ADR<1 instance is from the simulation with Fn 0.82 and CQ=1: in this case the airflow introduced from the step deviates towards the chine and escapes laterally.

The ADR>1 instance is from the simulation with Fn 1.64 and CQ=3: the airflow is now directed towards the transom, with almost no lateral escape.

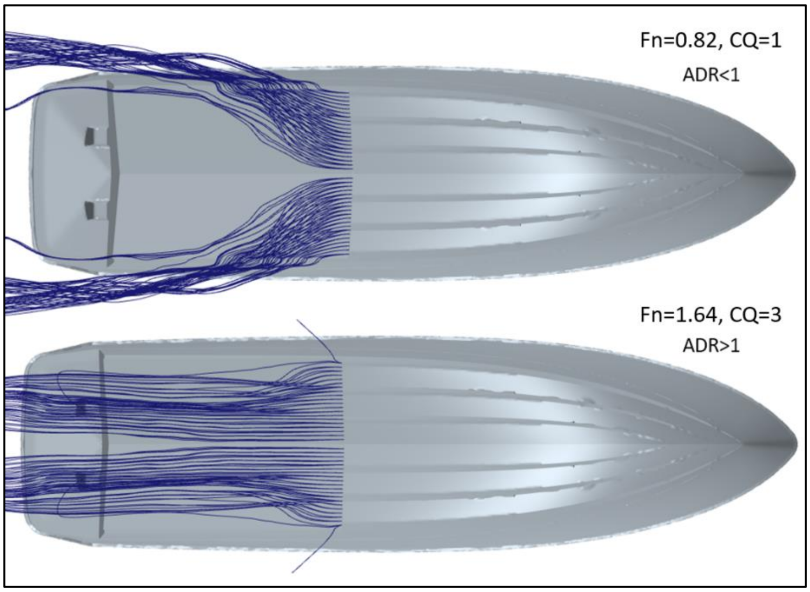

*Figure 41. Different behaviour of the airflow for ADR<1 and ADR>1 (bottom view)*

The trend of ADR for every velocity is reported in Figure 42. ADR is less than 1 only at Fn 0.55 and 0.82 for CQ1, CQ2 and CQ3; only for CQ1, ADR is less than 1 even at Fn 1.09. This means that the air layer is branching out in two sides, going towards the left and right chines. At Fn 1.09, ADR is greater than 1 for both CQ2 and CQ3; after this point, for every air velocity, ADR is greater than 1, increasing in its value from Fn 1.09 to 1.37 and decreasing from Fn 1.37 to 1.64.

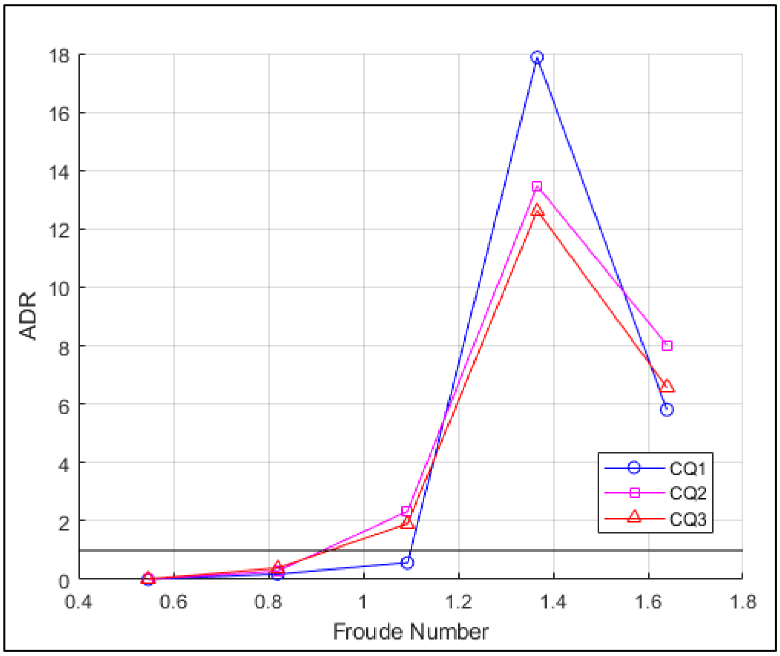

*Figure 42. Air Dissipation Ratio plot*

Another parameter defined is the Spray Rails Airflow Fraction (SRAF), which has been plotted in Figure 43 in percentage.

For every CQ, the trend of the SRAF is always increasing with the velocity of the hull, arriving to a maximum value at Fn 1.64. The trends for different CQs are practically overlapped until a velocity of 1.37; only at Fn 1.64 the trends diverge clearly, with the SRAF being approximately 26% for CQ1, 17% for CQ2 and around 15% for CQ3.

This means that the 26% of the air trapped under the hull comes from the spray rails for CQ1, but this effect becomes less important as the velocity of the injected air increments.

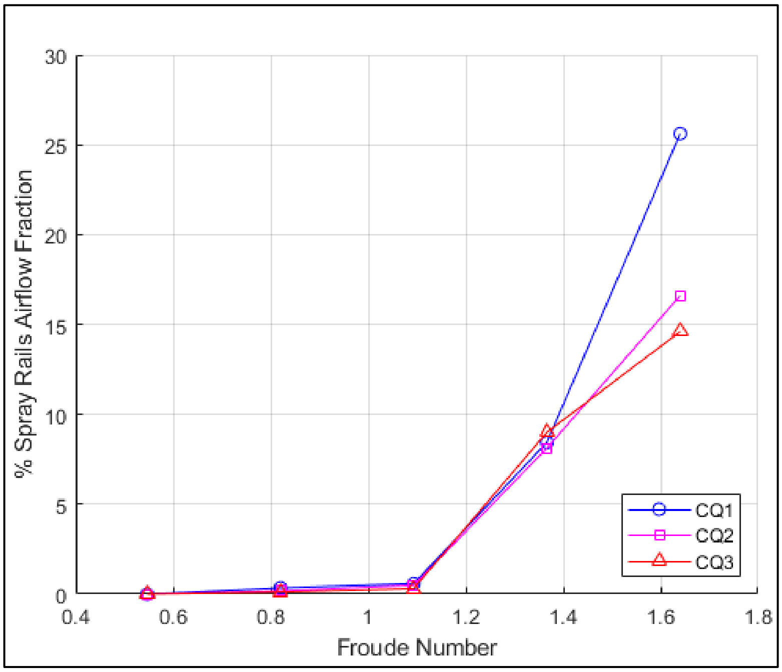

*Figure 43. Spray Rails Airflow Fraction plot*

Another data visualization method has been introduced using three of the main parameters that define the fluid dynamics behaviour of the stepped hull: the CQ, the hull velocity and the air volume trapped under the hull.

These values have been condensed in a 3D surface colored by the hull resistance values (Figure 44). Two main zones can be highlighted: a low-hull resistance zone and a high-hull resistance zone.

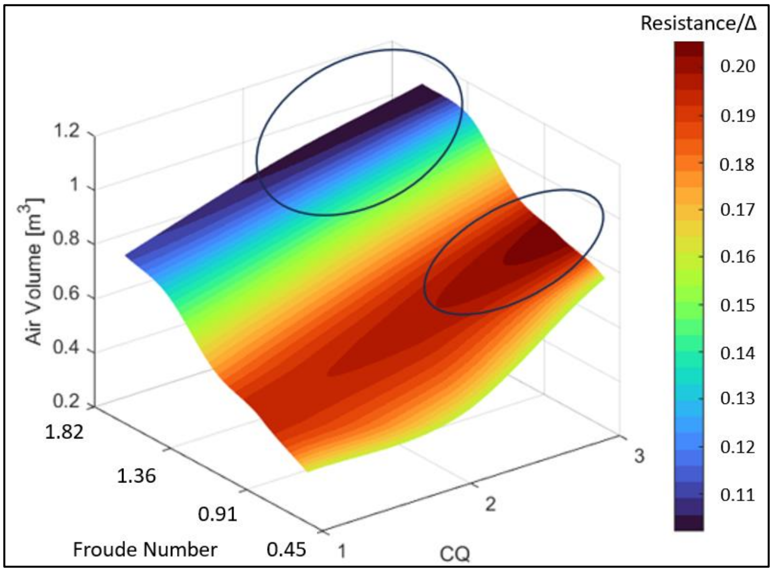

*Figure 44. 3D Surface Plot*

Looking at the colormap, the higher hull resistance is obtained for CQ3 at Fn 1.09, and it remains high even for the lower CQs at the same hull velocity. The hull resistance decreases with the increase of the hull velocity, reaching a minimum at Fn 1.64 between CQ2 and CQ3. At Fn 1.64, the effort of going from CQ2 to CQ3 is not justified by a major hull resistance reduction.

### 4.2.4 Propeller influence in planing conditions

The MRF rotating velocity has been set at 5000 rpm in order to get a hull velocity of 36 kn (Fn 1.82).

After stabilizing the hull at the desired velocity without air injection, simulations were made also at CQ1, CQ2 and CQ3 in order to obtain a resistance trend to compare with the simulations in the same conditions but without propellers.

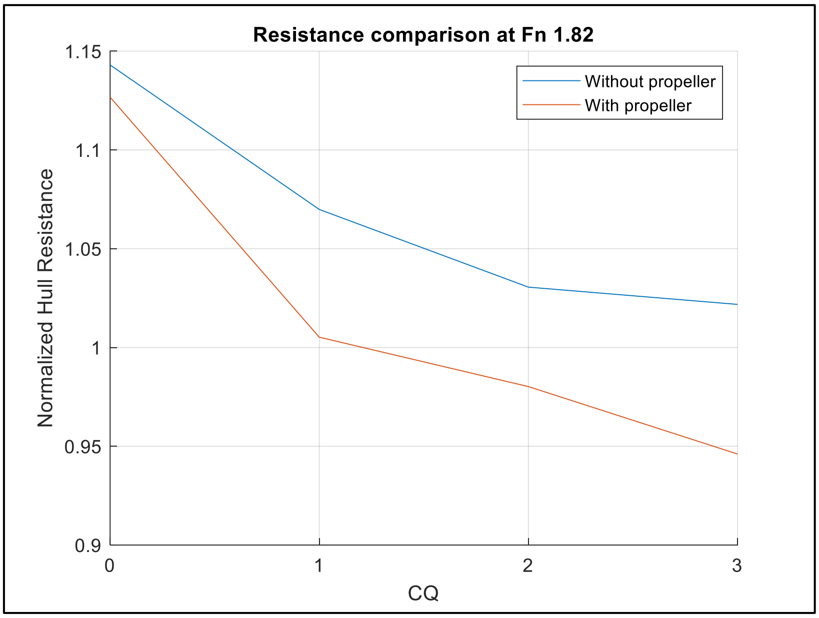

*Figure 45. Normalized Resistance comparison between towed and self-propelled hull*

The trend comparison in Figure 45 shows that the hull resistance decreases in the simulations with the propeller. Moreover, this difference increases with the increment in the CQ value.

The reason a hull with a moving propeller can have lower resistance compared to a towed hull, especially in the case of planing hulls, is related to the interaction between the hull and the propeller's thrust, as well as the flow dynamics around the hull.

Key factors to consider are the thrust deduction factor, the wake fraction and the planing dynamics.

The thrust deduction factor refers to the decrease in effective thrust due to the interaction between the hull and the propeller. When a propeller generates thrust, it affects the pressure distribution on the hull. This reduction in pressure near the stern can lower the overall hydrodynamic resistance because the propeller compensates for some of the pressure drag that the hull would otherwise experience if it were being towed. Essentially, the propeller is pushing the water behind the hull, reducing the negative pressure (suction) at the stern.

The wake fraction refers to the relative velocity of the water flow in the ship wake compared to the undisturbed water ahead. When the propeller is operating, it accelerates the water in the wake, potentially smoothing or altering the wake characteristics behind the hull.

This can reduce the resistance caused by turbulence and eddies that would otherwise increase drag if the hull were simply being towed without propulsion.

For planing hulls, the hull lifts out of the water as speed increases, significantly reducing the wetted surface area and thus lowering frictional resistance.

The interaction between the propeller thrust and hull lift can enhance this effect, as the propeller helps maintain a higher speed and further reduces the hull immersion. In contrast, a towed hull would not benefit from the same lifting forces and would experience higher resistance due to greater contact with the water.

From the results, it could be said the propellers are acting as flow extractors.

Air streamlines for these four simulations with propellers were extracted to evaluate their influence on air distribution.

In the CQ0 case (Figure 46) the streamlines appear to avoid the centreline of the hull, with a higher density on the outer propellers. This changes considering the simulations at higher CQs (Figure 47, Figure 48, Figure 49).

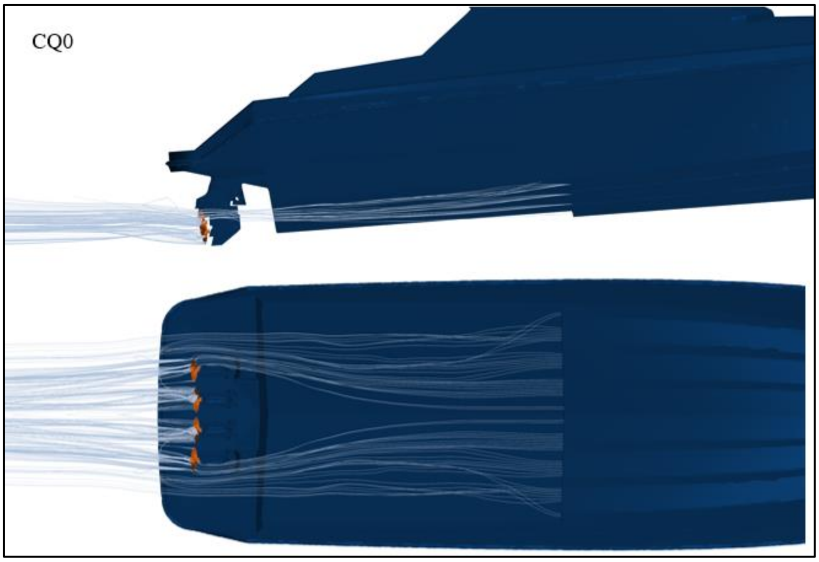

*Figure 46. Air streamlines for CQ0 with propeller*

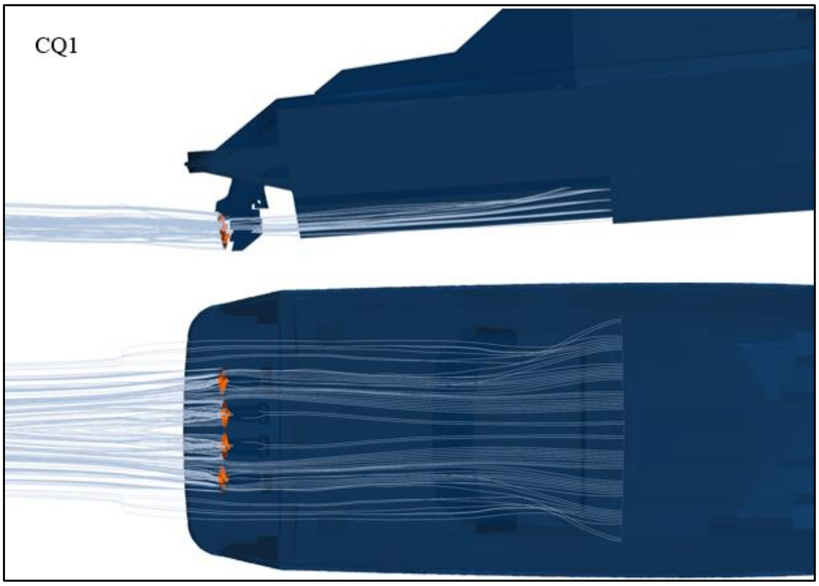

*Figure 47. Air streamlines for CQ1 with propeller*

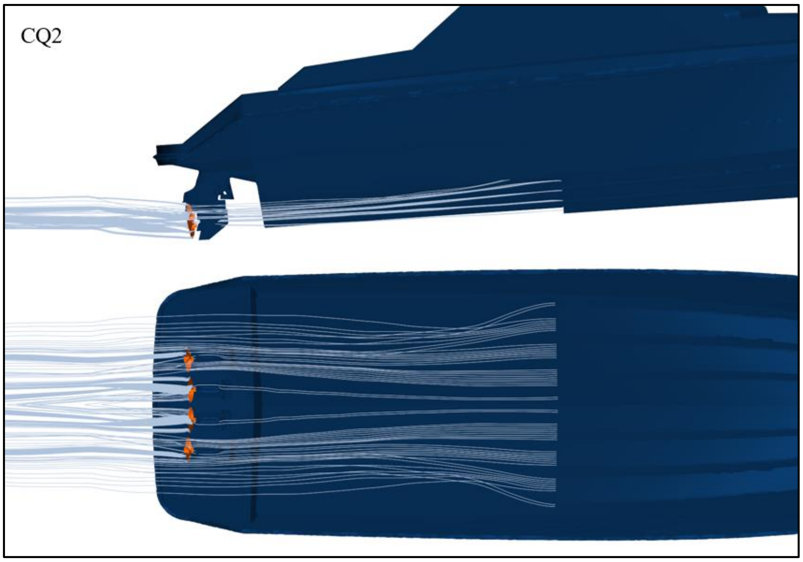

*Figure 48. Air streamlines for CQ2 with propeller*

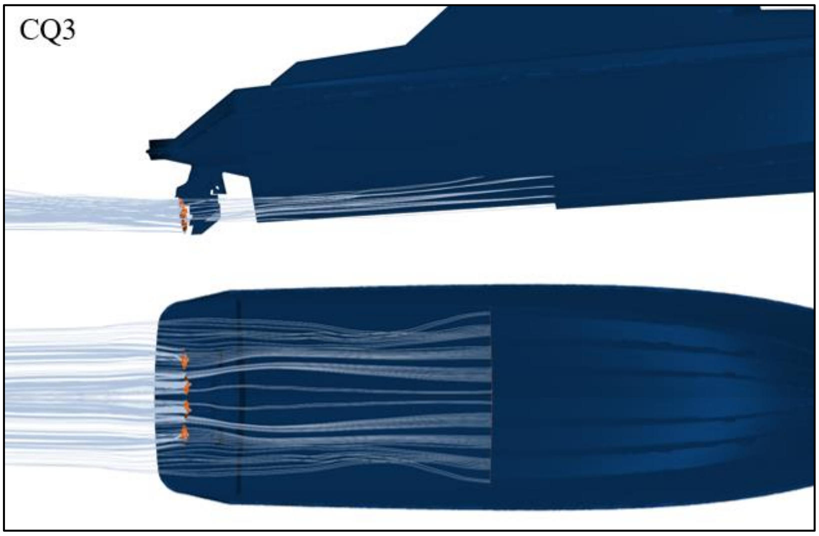

*Figure 49. Air streamlines for CQ3 with propeller*

The wake fraction related to the hull-propeller interaction can also be calculated.

The wake fraction ($w$) represents the average reduction in flow velocity in the wake region compared to the ship velocity. It is used to evaluate the influence of the wake on propulsive efficiency and can be defined as in Eq. 13.

$$w = 1 - \frac{V_w}{V} \tag{13}$$

where:

- $V_w$ is the average velocity of the flow in the wake, calculated as the mean velocity on the propeller disk ($V_{w1}$ will be referred to the propeller closer to the chine, $V_{w2}$ to the propeller near the centreline);

- $V$ is the ship velocity.

The wake velocity is obviously influenced by the air injection conditions. The values are listed in Table 19.

*Table 19. Wake fraction calculations*

| **V [m/s]** | **CQ** | **$V_{w1}$ [m/s]** | **$V_{w2}$ [m/s]** | **$w_1$** | **$w_2$** |
|---|---|---|---|---|---|
| 18.54 | 0 | 23.08 | 22.36 | -0.24 | -0.21 |
| 18.54 | 1 | 22.50 | 21.91 | -0.21 | -0.18 |
| 18.54 | 2 | 27.43 | 23.29 | -0.48 | -0.26 |
| 18.54 | 3 | 29.73 | 27.90 | -0.60 | -0.50 |

The propellers themselves do not directly reduce drag, but rather their interaction with the air injection system leads to a reduction in drag. This combined effect of air injection and propeller operation decreases the overall resistance of the hull. As a result, the wake fractions $w_1$ and $w_2$ (related to outer and centreline propellers respectively) can become negative, which is uncommon.

Normally, wake fraction values range between 0.1 and 0.4, as they reflect the reduction in flow velocity behind the hull. However, in this scenario, the interaction between the propellers and the injected air creates a unique situation where the flow in the wake region is accelerated, leading to a negative wake fraction.

Such negative values are unusual and indicate a highly efficient interaction between the air lubrication system and the propulsion system in reducing drag.

To understand why there was a reduction in resistance with the propellers, a comparison of trim between simulations without the propeller and those with the propeller was carried out (Table 20).

*Table 20. Trim comparison*

| **V [m/s]** | **CQ** | **τ without propellers [deg]** | **τ with propellers [deg]** |
|---|---|---|---|
| 18.54 | 0 | 4.2 | 3.5 |
| 18.54 | 1 | 3.8 | 3.4 |
| 18.54 | 2 | 3.7 | 3.4 |
| 18.54 | 3 | 3.7 | 3.3 |

The results showed that the trim was lower and more stable across different CQ values. This suggests that the thrust from the propellers helped to straighten and stabilize the ship, thus reducing the overall resistance.

The propellers likely reduced trim because the thrust generated at the stern exerts an upward force, particularly at higher speeds.

This counteracts the bow-up moment, which often leads to increased drag, especially in planing or near-planing conditions.

By reducing the trim angle, the ship wetted surface area is minimized, resulting in less drag and improved overall efficiency.

# 5. Future developments

Several research topics can build on this study. One promising direction is expanding the investigation into the scalability of air distribution beneath the hull by considering additional intermediate scales between those tested, as well as exploring different air injection conditions. This would allow for the collection of more comprehensive data and the development of procedures that incorporate Bond number corrections, similar to the ITTC Reynolds number corrections.

The study of the propeller influence on a planing hull can also be deepened by generating resistance curves for a self-propelled hull across different Froude numbers. Additionally, the novel method for visualizing the air cushion proposed in this thesis can be applied to simulations with the propeller, enabling the observation of local changes in air distribution beneath the hull.

# 6. Conclusions

This thesis addressed current topics of interest in naval architecture and numerical simulations. Starting with a thorough review of the state-of-the-art technologies for drag reduction through air lubrication, an initial study was conducted on a planing hull for which towing tank tests were available. A 2-degrees-of-freedom, multiphase CFD model was validated, allowing for a preliminary analysis of the impact of scale on the distribution of air injected beneath the hull. The results revealed that the shape of the airflow under the hull changes significantly with geometric scaling, although this effect diminishes with increasing Froude numbers. The primary factor driving this behaviour is the Bond number, which reflects the influence of surface tension, is inherently linked to scaling, and has not previously been considered in the literature to describe such phenomena.

Using the same validated CFD model, a second planing hull, which initially did not include forced air injection, was modified by introducing a step and transforming it into an Air Cavity Ship. The hydrodynamic characteristics of this modified hull were thoroughly studied to assess drag, trim, and wetted surface at various Froude numbers, covering operational conditions from displacement mode to planing. The characterization was conducted both without air injection and with varying injection rates. Two new coefficients were defined: the Air Direction

Ratio, which indicates the preferential direction of ventilation beneath the hull, and the Spray Rails Airflow Fraction, which measures how much air is drawn from the spray rails compared to the forced injection. A novel method for visualizing the local air cushion thickness beneath the hull was introduced, adding a three-dimensional perspective to assessments previously made using 2D air volume fraction maps. Lastly, CFD simulations were performed to evaluate the hull-propeller interaction, providing valuable insights into the thrust deduction factor and the wake volumetric fraction, contributing to a more comprehensive understanding of the system's performance.

# References

1. Tsai, J.-F., Chen, C.-C.: Boundary Layer Mixture Model for a Microbubble Drag Reduction Technique. Int Sch Res Notices. (2011). https://doi.org/10.5402/2011/405701.
2. Sanders, W.C., Winkel, E.S., Dowling, D.R., Perlin, M., Ceccio, S.L.: Bubble friction drag reduction in a high-Reynolds-number flat-plate turbulent boundary layer. J Fluid Mech. (2006). https://doi.org/10.1017/s0022112006008688.
3. Elbing, B.R., Winkel, E.S., Lay, K.A., Ceccio, S.L., Dowling, D.R., Perlin, M.: Bubble-induced skin-friction drag reduction and the abrupt transition to air-layer drag reduction. J Fluid Mech. (2008). https://doi.org/10.1017/s0022112008003029.
4. Sayyaadi, H., Nematollahi, M.: Determination of optimum injection flow rate to achieve maximum micro bubble drag reduction in ships; an experimental approach. Scientia Iranica. 20, 535–541 (2013). https://doi.org/10.1016/J.SCIENT.2013.05.001.
5. Park, H.J., Tasaka, Y., Oishi, Y., Murai, Y.: Drag reduction promoted by repetitive bubble injection in turbulent channel flows. International Journal of Multiphase Flow. 75, 12–25 (2015).

https://doi.org/10.1016/J.IJMULTIPHASEFLOW.2015.05.003.

6. Jacob, B., Olivieri, A., Miozzi, M., Miozzi, M., Miozzi, M., Campana, E.F., Piva, R.: Drag reduction by microbubbles in a turbulent boundary layer. Physics of Fluids. (2010). https://doi.org/10.1063/1.3492463.
7. Guin, M.M., Kato, H., Yamaguchi, H., Maeda, M., Miyanaga, M.: Reduction of skin friction by microbubbles and its relation with near-wall bubble concentration in a channel. J Mar Sci Technol. 1, 241–254 (1996). https://doi.org/10.1007/BF02390723/METRICS.
8. Yanuar, Gunawan, Gunawan, Gunawan, Sunaryo, Jamaluddin, A.: Micro-bubble drag reduction on a high speed vessel model. Journal of Marine Science and Application. (2012). https://doi.org/10.1007/s11804-012-1136-z.
9. Murai, Y., Fukuda, H., Oishi, Y., Kodama, Y., Yamamoto, F.: Skin friction reduction by large air bubbles in a horizontal channel flow. International Journal of Multiphase Flow. (2007). https://doi.org/10.1016/j.ijmultiphaseflow.2006.08.008.
10. Kodama, Y., Kakugawa, A., Takahashi, T., Kawashima, H.: Experimental study on microbubbles and their

applicability to ships for skin friction reduction. Int J Heat Fluid Flow. (2000). https://doi.org/10.1016/s0142-727x(00)00048-5.

11. Madavan, N.K., Deutsch, S., Merkle, C.L.: Reduction of turbulent skin friction by microbubbles. Phys Fluids. 27, 356–363 (1984). https://doi.org/10.1063/1.864620.

12. Kumagai, I., Takahashi, Y., Murai, Y.: Power-saving device for air bubble generation using a hydrofoil to reduce ship drag: Theory, experiments, and application to ships. Ocean Engineering. (2015). https://doi.org/10.1016/j.oceaneng.2014.11.019.

13. Tanaka, T., Oishi, Y., Park, H.J., Tasaka, Y., Murai, Y., Kawakita, C.: Downstream persistence of frictional drag reduction with repetitive bubble injection. Ocean Engineering. 272, (2023). https://doi.org/10.1016/J.OCEANENG.2023.113807.

14. Jang, J., Choi, S.H., Ahn, S.M., Kim, B., Seo, J.S.: Experimental investigation of frictional resistance reduction with air layer on the hull bottom of a ship. International Journal of Naval Architecture and Ocean Engineering. 6, 363–379 (2014). https://doi.org/10.2478/IJNAOE-2013-0185.

15. Hao, W.U., Yongpeng, O., Qing, Y.E.: Experimental study of air layer drag reduction on a flat plate and

bottom hull of a ship with cavity. Ocean Engineering. 183, 236–248 (2019). https://doi.org/10.1016/J.OCEANENG.2019.04.088.

16. Wu, H., Ou, Y. peng: Experimental Study of Air Layer Drag Reduction with Bottom Cavity for A Bulk Carrier Ship Model. China Ocean Engineering. 33, 554–562 (2019). https://doi.org/10.1007/S13344-019-0053-1/METRICS.

17. Yanuar, Waskito, K.T., Pratama, S.Y., Candra, B.D., Rahmat, B.A.: Comparison of Microbubble and Air Layer Injection with Porous Media for Drag Reduction on a Self-propelled Barge Ship Model. Journal of Marine Science and Application. 17, 165–172 (2018). https://doi.org/10.1007/S11804-018-0028-2/METRICS.

18. Aljallis, E., Sarshar, M.A., Datla, R., Sikka, V., Jones, A., Choi, C.H.: Experimental study of skin friction drag reduction on superhydrophobic flat plates in high Reynolds number boundary layer flow. Physics of Fluids. 25, (2013). https://doi.org/10.1063/1.4791602/257816.

19. Slyozkin, A., Atlar, M., Sampson, R., Seo, K.C.: An experimental investigation into the hydrodynamic drag reduction of a flat plate using air-fed cavities. Ocean

Engineering. 76, 105–120 (2014). https://doi.org/10.1016/J.OCEANENG.2013.10.013.

20. Butterworth, J., Atlar, M., Shi, W.: Experimental analysis of an air cavity concept applied on a ship hull to improve the hull resistance. Ocean Engineering. 110, 2–10 (2015). https://doi.org/10.1016/J.OCEANENG.2015.10.022.

21. De Marco, A., Mancini, S., Miranda, S., Scognamiglio, R., Vitiello, L.: Experimental and numerical hydrodynamic analysis of a stepped planing hull. Applied Ocean Research. 64, 135–154 (2017). https://doi.org/10.1016/J.APOR.2017.02.004.

22. Cucinotta, F., Guglielmino, E., Sfravara, F.: An experimental comparison between different artificial air cavity designs for a planing hull. Ocean Engineering. 140, 233–243 (2017). https://doi.org/10.1016/J.OCEANENG.2017.05.028.

23. Song, L., Yu, J., Yu, Y., Wang, Z., Wu, S., Gao, R.: An Experimental Study on the Resistance of a High-Speed Air Cavity Craft. Journal of Marine Science and Engineering 2023, Vol. 11, Page 1256. 11, 1256 (2023). https://doi.org/10.3390/JMSE11071256.

24. Zhao, X., Zong, Z., Jiang, Y., Pan, Y.: Numerical simulation of micro-bubble drag reduction of an

axisymmetric body using OpenFOAM. Journal of Hydrodynamics. (2019). https://doi.org/10.1007/s42241-018-0118-2.

25. Mohanarangam, K., Mohanarangam, K., Cheung, S.C.P., Zhang, L., Tu, J., Chen, L.: Numerical simulation of micro-bubble drag reduction using population balance model. Ocean Engineering. (2009). https://doi.org/10.1016/j.oceaneng.2009.05.001.

26. Gamal, M., Kotb, M., Ahmed, N., Khaled, E., Elsherbiny, K.: Numerical investigations of micro bubble drag reduction effect for container ships. Marine Systems & Ocean Technology. (2021). https://doi.org/10.21203/rs.3.rs-641471/v1.

27. Xia, W., Song, W., Wang, C., Yi, W., Meng, Q., Deng, H.: Microbubbles drag reduction characteristics of underwater vehicle during pitching movement. Ocean Engineering. 285, (2023). https://doi.org/10.1016/J.OCEANENG.2023.115350.

28. An, H., Yang, P., Zhang, H., Liu, X.: Numerical Study of the Influence of the Type of Gas on Drag Reduction by Microbubble Injection. Inventions. 9, (2024). https://doi.org/10.3390/INVENTIONS9010007.

29. Xiaosong, Z., Jian-hua, W., Decheng, W.: Euler-Lagrange study of bubble drag reduction in turbulent

channel flow and boundary layer flow. Physics of Fluids. (2020). https://doi.org/10.1063/1.5141608.

30. Xu, J., Maxey, M.R., Karniadakis, G.E.: Numerical simulation of turbulent drag reduction using micro-bubbles. J Fluid Mech. 468, 271–281 (2002). https://doi.org/10.1017/S0022112002001659.

31. Pang, M., Wei, J., Yu, B.: Numerical study on modulation of microbubbles on turbulence frictional drag in a horizontal channel. Ocean Engineering. (2014). https://doi.org/10.1016/j.oceaneng.2014.02.012.

32. Montazeri, M., Alishahi, M.: An efficient method for numerical modeling of thin air layer drag reduction on flat plate and prediction of flow instabilities. Ocean Engineering. (2019). https://doi.org/10.1016/j.oceaneng.2019.03.016.

33. Zhang, J., Yang, S., Liu, J., Liu, J.: Numerical investigation of frictional drag reduction with an air layer concept on the hull of a ship. Journal of Hydrodynamics. (2019). https://doi.org/10.1007/s42241-019-0063-8.

34. Hao, W.U., Yongpeng, O.U.: Numerical simulation of air layer morphology on flat bottom plate with air cavity and evaluation of the drag reduction effect. International Journal of Naval Architecture and Ocean Engineering. (2019). https://doi.org/10.1016/j.ijnaoe.2018.09.005.

35. Ye, Q., Ou, Y., Xiang, G., Chen, J.: Numerical Study on the Influence of Water Depth on Air Layer Drag Reduction. Applied Sciences. 14, 431 (2024). https://doi.org/10.3390/APP14010431.

36. Zhang, X.: CFD STUDY OF AIR-LAYER DRAG REDUCTION ON A PLATE WITH DIFFERENT KINDS OF CAVITY DESIGN. null. (2020). https://doi.org/null.

37. Xu, K., Su, X., Bensow, R., Krajnovic, S.: Large eddy simulation of ship airflow control with steady Coanda effect. Physics of Fluids. 35, (2023). https://doi.org/10.1063/5.0127560.

38. Kim, D., Moin, P., Kim, D., Moin, P.: Direct Numerical Simulation of Air Layer Drag Reduction over a Backward-facing Step. APS. 63, EU.008 (2010).

39. Lotfi, P., Ashrafizaadeh, M., Kowsari-Esfahan, R., Esfahan, R.K.: Numerical investigation of a stepped planing hull in calm water. Ocean Engineering. (2015). https://doi.org/10.1016/j.oceaneng.2014.11.022.

40. Cucinotta, F., Guglielmino, E., Sfravara, F., Strasser, C.: Numerical and experimental investigation of a planing Air Cavity Ship and its air layer evolution. Ocean Engineering. 152, 130–144 (2018). https://doi.org/10.1016/J.OCEANENG.2018.01.071.

41. Cucinotta, F., Nigrelli, V., Sfravara, F.: Numerical prediction of ventilated planing flat plates for the design of Air Cavity Ships. International Journal on Interactive Design and Manufacturing (ijidem). (2018). https://doi.org/10.1007/s12008-017-0396-x.

42. Cucinotta, F., Guglielmino, E., Sfravara, F.: A critical CAE analysis of the bottom shape of a multi stepped air cavity planing hull. Applied Ocean Research. 82, 130–142 (2019). https://doi.org/10.1016/J.APOR.2018.11.003.

43. Cucinotta, F., Mancini, D., Sfravara, F., Tamburrino, F.: The Effect of Longitudinal Rails on an Air Cavity Stepped Planing Hull. J Mar Sci Eng. 9, (2021). https://doi.org/10.3390/JMSE9050470.

44. Fang, H., Chen, Z., Chen, C., Sun, S., Wang, X., Wu, D., Qin, S.: On the drag reduction and heeling stability of a heeled planing air cavity hull. Ocean Engineering. 283, (2023). https://doi.org/10.1016/J.OCEANENG.2023.115087.

45. Mukha, T., Bensow, R.: Large-Eddy Simulation of an Internal Ship Air Cavity in Model Scale. null. (2018). https://doi.org/null.

46. Matveev, K.I., Matveev, K.I., Matveev, K.I., Matveev, K.I.: On the limiting parameters of artificial cavitation.

Ocean Engineering. (2003). https://doi.org/10.1016/s0029-8018(02)00103-8.

47. Yang, D., Sun, Z., Jiang, Y., Gao, Z.: A Study on the Air Cavity under a Stepped Planing Hull. Journal of Marine Science and Engineering 2019, Vol. 7, Page 468. 7, 468 (2019). https://doi.org/10.3390/JMSE7120468.

48. Amromin, E.L.: Analysis of interaction between ship bottom air cavity and boundary layer. Applied Ocean Research. 59, 451–458 (2016). https://doi.org/10.1016/J.APOR.2016.03.009.

49. Wheeler, M.P., Ryan, P., Cimolin, F.: Using VOF Slip Velocity to Improve Productivity of Planing Hull CFD Simulations. SNAME International Conference on Fast Sea Transportation 2021. FAST 2021. (2021). https://doi.org/10.5957/FAST-2021-013.

50. Matveev, K.I.: Computational Simulations of Wide-Beam Air-Cavity Hull in Waves. SNAME International Conference on Fast Sea Transportation 2021. FAST 2021. (2021). https://doi.org/10.5957/FAST-2021-006.

51. Cignoni, P., Rocchini, C., Scopigno, R.: Metro: measuring error on simplified surfaces. In: Computer Graphics Forum. pp. 167–174. Blackwell Publishers (1998).

52. Schlichting, H., Gersten, K.: Boundary-Layer Theory. Boundary-Layer Theory. 1–799 (2016). https://doi.org/10.1007/978-3-662-52919-5/COVER.